

# GASS High Velocity Clouds in the Region of the Magellanic Leading Arm

Bi-Qing For<sup>1</sup>, Lister Staveley-Smith<sup>1</sup>, N. M. McClure-Griffiths<sup>2</sup>

<sup>1</sup>*International Centre for Radio Astronomy Research, University of Western Australia, 35 Stirling Hwy, Crawley, WA, 6009, Australia; biqing.for@uwa.edu.au*

<sup>2</sup>*CSIRO Astronomy and Space Science, Epping, NSW, 1710, Australia*

## ABSTRACT

We present a catalog of high-velocity clouds in the region of the Magellanic Leading Arm. The catalog is based on neutral hydrogen (HI) observations from the Parkes Galactic All-Sky Survey (GASS). Excellent spectral resolution allows clouds with narrow-line components to be resolved. The total number of detected clouds is 419. We describe the method of cataloging and present the basic parameters of the clouds. We discuss the general distribution of the high-velocity clouds and classify the clouds based on their morphological type. The presence of a significant number of head-tail clouds and their distribution in the region is discussed in the context of Magellanic System simulations. We suggest that ram-pressure stripping is a more important factor than tidal forces for the morphology and formation of the Magellanic Leading Arm and that different environmental conditions might explain the morphological difference between the Magellanic Leading Arm and Magellanic Stream. We also discuss a newly identified population of clouds that forms the LA IV and a new diffuse bridge-like feature connecting the LA II and III complexes.

*Subject headings:* Galaxy: halo – intergalactic medium – ISM: HI– Magellanic Clouds

## 1. INTRODUCTION

Some atomic neutral hydrogen (HI) concentrations surrounding our Galaxy have anomalous velocities that are forbidden by a simple Galactic rotation model. These so-called

anomalous-velocity clouds contain HI without a stellar counterpart. They can be classified into two velocity based groups: intermediate velocity clouds (IVCs; Münch & Zirin 1961; Blaauw & Tolbert 1966); high-velocity clouds (HVCs; Muller et al. 1963). The classification of IVCs and HVCs is based on the deviation velocity, which is defined as the smallest difference between the velocity of the cloud and the Galactic rotational velocity (Wakker 1991). High-velocity clouds are particularly interesting because they are thought to represent the flow of baryons in or out of the Galactic disk, which influences the formation and evolution of our Galaxy. Despite being important in the context of galaxy formation and evolution, their origin and physical characteristics are still under debate.

Possible explanations of the origin of HVCs can be traced back to an early study by Oort (1966). One of his hypotheses suggested that the HVCs have an extragalactic origin. This hypothesis received more recent support from Blitz et al. (1999) with the argument that HVCs are dark matter dominated clouds in the Local Group with distances of hundreds of kiloparsecs. A similar study by Braun & Burton (1999) also claimed that compact and isolated HVCs lie at extragalactic distances. Another popular HVC origin hypothesis is the Galactic fountain model, in which the gas is blown out of the disk by supernovae, cools and then rains back down (see e.g., Houck & Bregman 1990). In this scenario, the fountain gas can rise as high as  $\sim 10$  kpc above the disk (de Avillez 2000).

The previous large-scale surveys, the Leiden–Argentine–Bonn Galactic HI survey (LAB; Kalberla et al. 2005) and the HI Parkes All-Sky Survey (HIPASS; Barnes et al. 2001) have provided opportunities to study HVCs on a global scale to assist in the understanding of their origin and physical properties (see e.g., Wakker & van Woerden 1991; Putman et al. 2002). LAB covered the entire sky with an angular resolution of  $36'$  and a spectral resolution of  $1.3 \text{ km s}^{-1}$ . HIPASS was conducted with a better angular resolution ( $16'$ ) but lower spectral resolution ( $18 \text{ km s}^{-1}$ ). A comprehensive catalog of Southern HVCs based on the HIPASS data was presented in Putman et al. (2002), hereafter P02. The catalog covers the high-velocity HI sky south of declination  $+2^\circ$  and within the Local Standard of Rest velocity ( $V_{LSR}$ ) range of  $+500$  to  $-500 \text{ km s}^{-1}$ . It provides the spatial and kinematic distributions as well as the properties of high-velocity clouds. Even though the P02 catalog includes a complete census of HVCs south of declination  $+2^\circ$ , the nature of the in-scan bandpass calibration technique filtered out some of large-scale structure of the Milky Way and the Magellanic System.

Among HVC complexes, the Magellanic System is the most interesting given that it is the only closest extragalactic gaseous stream to our Galaxy. The Magellanic System consists of a coherent gas stream originating from the Magellanic Clouds (MCs), i.e., Magellanic Stream (MS) and Leading Arm (LA) (Mathewson et al. 1974). The MS is trailing the MCs

and has a complex filamentary structure. On the other hand, the LA is clumpy and dominated by three distinctive large complexes, namely the LA I, LA II and LA III (Putman et al. 1998; Brüns et al. 2005). An extended feature of the MS has recently been discovered by Nidever et al. (2010), which reveals the total length of the MS as  $\sim 200^\circ$  across the sky. Another recent report of several filaments that are aligned with the MS also suggests that MS is wider than previously thought (Westmeier et al. 2011).

The formation of the MS and LA is generally believed to have been caused by the tidal interaction between the Milky Way and Magellanic Clouds. Theoretical models with tidal stripping, gravitational and hydrodynamical interactions can reproduce global observed HI column density and velocity distributions (see e.g., Connors et al. 2006; Mastropietro et al. 2005). However, these models do not provide a satisfactory explanation for the formation mechanism of the MS and LA. With the recent Hubble Space Telescope proper motion measurements of the MCs (Kallivayalil et al. 2006a,b), a new unbound orbit for the MCs with a first passage scenario was proposed by Besla et al. (2007). The result is surprising given that the new orbit does not provide sufficient time for tidal and ram-pressure stripping mechanisms to produce the MS (Stanimirović et al. 2008). To circumvent the problem raised by the first passage scenario, Nidever et al. (2008) proposed a new blowout hypothesis. They suggested that the supergiant shells in the dense southeast HI overdensity region are blown out from the Large Magellanic Cloud (LMC) to larger radii where ram-pressure and/or tidal forces can be more easier to strip the gas and form the MS and LA. Nevertheless, with recent higher measurements of the Milky way’s circular velocity (e.g., 251 km s<sup>-1</sup>; Reid & Brunthaler 2004) compared to the IAU standard of 220 km s<sup>-1</sup>, there remains the distinct possibility that a multi-orbit scenario is plausible (Shattow & Loeb 2009). Recent multi-orbit simulations have also reproduced the observed structure of the MS, including bifurcation of the two filaments, whilst remaining consistent with the proper motion data (Diaz & Bekki 2011a,b). However, none of the theoretical models to date have been able to accurately reproduce the observed structure of the LA.

To study the Magellanic System in detail, Brüns et al. (2005) carried out a narrow-band Parkes HI survey. In contrast to HIPASS, which was not designed to accurately measure low-velocity Galactic HI gas, the survey was designed exclusively to study the Magellanic System. The Brüns’ survey has a similar angular resolution and spectral resolution to the Galactic All-Sky Survey (GASS; McClure-Griffiths et al. 2009; Kalberla et al. 2010) (see §2), but with limited sky coverage. Another high-resolution HI study that concentrated on the northern tip of the MS was carried out by Stanimirović et al. (2008). This study was part of the Galactic studies with Arecibo *L*-band Feed Array (GALFA).

The current work utilizes the GASS data for studying the general distribution and

morphological types of HVC in the region of the Magellanic Leading Arm. The GASS data have better sky coverage than the Brüns’ survey and higher spectral resolution than HIPASS. The study of HVCs in the vicinity of the LA gives us clues to understand: (1) the formation of the LA; (2) the physical properties of the HVCs; and most importantly, (3) the role of infalling gas in the context of galaxy evolution and formation. In §2, we describe the GASS data and the procedures for cloud search algorithms. We present the catalog and the general distribution of clouds in §3 and §4. Classification of the clouds and interpretation of the distribution for each group are given in §5. Finally, we report on the new extended features of the Magellanic Leading Arm and discuss the implications of HVCs for the formation and origin of the LA in §6. Conclusions are drawn in §7.

## 2. DATA

The neutral hydrogen data employed here are from GASS. This survey covers the entire Southern sky to declination  $+1^\circ$  and  $V_{LSR}$  from  $-400$  to  $+500$   $\text{km s}^{-1}$ . The data from the GASS second data release<sup>1</sup> have been corrected for stray radiation, have an angular resolution of  $\sim 16'$ , a brightness temperature ( $T_B$ ) sensitivity of 57 mK, a channel width of  $0.82$   $\text{km s}^{-1}$  and a spectral resolution of  $1$   $\text{km s}^{-1}$ . For a typical HVC of  $15$   $\text{km s}^{-1}$  line width in our sample, the  $1\sigma$  HI column density ( $N_{\text{HI}}$ ) sensitivity is  $3.5 \times 10^{17}$   $\text{cm}^{-2}$ . We refer the reader to McClure-Griffiths et al. (2009) and Kalberla et al. (2010) for a detailed description of the observing technique and data reduction.

To create a catalog of HVCs in the region of the Magellanic Leading Arm, we extracted a GASS data cube within the area of  $-30^\circ \lesssim b \lesssim +40$  and  $240^\circ \lesssim l \lesssim 315^\circ$ , and covered the velocity range of  $0$  to  $450$   $\text{km s}^{-1}$ . Before performing any cloud search algorithm, we examined the data cube and determined the velocity range that solely contain Galactic HI emission,  $0$   $\text{km s}^{-1} \leq V_{LSR} < 150$   $\text{km s}^{-1}$ . Beyond this velocity range, there is a mix of Galactic HI emission and possible HI emission that is associated with the MCs. Brüns et al. (2005) analyzed the HVCs in the region of the LA by using different velocity ranges within certain Galactic latitudes. Due to the difficulty in distinguishing the Galactic HI and HI emission originating from the MCs, we deliberately masked out the regions of  $-20^\circ \lesssim b \lesssim +20^\circ$  and  $l < 310^\circ$  between  $150$  and  $190$   $\text{km s}^{-1}$  for our analysis. Other small regions of Galactic HI emission in higher velocity channels, as determined by eye, were also masked. An integrated HI column density map of HVCs in the region of the LA over the velocity interval of  $150$  to  $450$   $\text{km s}^{-1}$  is shown in Figure 1.

---

<sup>1</sup><http://www.astro.uni-bonn.de/hisurvey/gass/>

## 2.1. Source Finding

We employed the source finding software, *Duchamp*<sup>2</sup> V1.1.13, developed by Whiting (2012). It is a 3-dimensional source finding software that provides flexibility for the user to control all relevant input parameters. To enhance the detectability of fainter sources, it implements optional noise reduction routines, such as the *à trous* wavelet reconstruction technique (Starck & Murtagh 1994) and the spatial or spectral smoothing routine. A full description of *Duchamp* is given in Whiting (2012). Here we describe the basic flow of the program with the applied input parameters:

- Spectral channels with Milky Way emission,  $0 \text{ km s}^{-1} \leq V_{LSR} < 150 \text{ km s}^{-1}$ , were flagged (see §2) and were excluded when performing the search.
- The cube was reconstructed via the *à trous* wavelet reconstruction method. It determined the amount of structures at various scales, and random noise was removed from the cube based on a user defined threshold.
- We did not use the spectral or spatial smoothing to remove the random noise because tests had shown that the *à trous* wavelet reconstruction method yielded a better source detection rate.
- A fixed threshold of  $\sim 2\sigma$  above the background noise (57 mK) was specified for the source finding. We did not adopt the auto-threshold determining scheme of *Duchamp*.
- *Duchamp* searched for sources one channel at a time using the defined threshold. Sources were confirmed only if they extend to a minimum of 5 channels in velocity space and 10 pixels spatially.
- Subsequently, detections were compared to earlier detected sources and either combined with a neighboring source or added to the list.

We also performed the source finding using *Clumpfind*. *Clumpfind* is a cloud finding algorithm developed to quantify the fragmentation or clumpiness of molecular clouds (Williams et al. 1994). The routine contours the data with user defined root mean square noise of the observations and interval, then searches for peaks of emission to locate the clumps at each contour level and splits any blended clumps with a friends-of-friends algorithm. We chose to adopt *Duchamp* for this study as it breaks sources into fewer components.

---

<sup>2</sup>Available at <http://www.atnf.csiro.au/computing/software/duchamp/>

### 3. CATALOG

We present the basic information of the sources in Table 1. The catalog includes the object identification number in column 1; the designation with a prefix of HVC for high-velocity clouds and GLX for galaxies followed by the Galactic longitude, Galactic latitude and the velocity in the Local Standard of Rest reference frame ( $V_{LSR}$ ) of the source in column 2;  $V_{LSR}$  in column 3; the velocity in the Galactic Standard of Rest reference frame ( $V_{GSR}$ ), defined by  $V_{GSR} = 220 \cos b \sin l + V_{LSR}$ ; the velocity in the Local Group Standard of Rest reference frame ( $V_{LGSR}$ ), defined by  $V_{LGSR} = V_{GSR} - 62 \cos l \cos b + 40 \sin l \cos b - 35 \sin b$  (Braun & Burton 1999) in columns 5–6; velocity FWHM, measured at 50% of peak flux in column 6; integrated flux, peak  $T_B$  and peak  $N_{HI}$  in columns 7–9; semi-major axis, semi-minor axis and position angle in columns 10–12; warning flag in column 13; and classification in column 14 (see §5). Most of the parameters are derived from *Duchamp*, with the exception of angular sizes and peak HI column density, which are determined independently. Sources that straddle our velocity boundary and masked Milky Way emission boundary are included in the catalog but their physical parameters cannot be determined accurately and are therefore not listed in the table. We present the examples of integrated HI column density maps and LSR velocity maps of individual cloud in Figures 2 and 3.

With the procedures described in §2.1, we found 838 sources with *Duchamp*. False detections caused by background artifacts were eliminated from the initial search. The positions of final detected sources were subsequently examined using the NASA/IPAC Extragalactic Database with a 16' search radius to identify any galaxy. The final count includes a total of 419 HVCs and 12 galaxies in the region of the Magellanic Leading Arm. We determined the peak  $N_{HI}$  by locating the brightest pixel in the integrated HI column density map of each source. To determine the angular size of the HVCs, we used 2-dimensional Gaussian and elliptical fitting, which gave the semi-major axis, semi-minor axis and position angle. A detailed investigation and discussion of advantages and disadvantages for both fitting methods, applied to molecular cloud catalogs, is given in Kerton et al. (2003). We elect to use the results from the 2-dimensional Gaussian fitting for the catalog. Due to the inaccuracy of the position angle in some cases, caution is needed in interpreting this parameter.

The reliability of *Duchamp* for parametrization of sources has been extensively tested on artificial sources of various parameters by Westmeier et al. (2011). Their tests show that the integrated flux ( $F_{int}$ ) measured by *Duchamp* is systematically too low for faint sources. To demonstrate how this systematic error affects the integrated flux of real sources found in our catalog, we measured the  $F_{int}$  with a better parametrization algorithm. This stand-alone parametrization algorithm uses the position output from *Duchamp* to find sources in the data cube. An integrated map is created and an ellipse fitted to the source. Subsequently, the

ellipse is grown in size until the measured integrated flux reaches a maximum. The  $F_{\text{int}}$  is then measured within the final ellipse. In Figure 4, we show that the ratios of our measured  $F_{\text{int}}$  to  $F'_{\text{int}}$  as measured by *Duchamp* as a function of measured *Duchamp*  $F'_{\text{int}}$  in various bins. Parametrization of large and extended or close kind confused sources is challenging (T. Westmeier, priv communication). Thus, these sources are excluded from the comparison. The red, dotted line is a fit to the data points, which represents the underestimated factor for a given  $F'_{\text{int}}$  as measured by *Duchamp*. We conclude that *Duchamp* produces accurate measurements of  $F'_{\text{int}}$  for sources with  $F'_{\text{int}} \gtrsim 80 \text{ Jy km s}^{-1}$  in our catalog. We correct all the  $F'_{\text{int}}$  values measured by *Duchamp* based on the fitting function.

Corrections are not necessary for peak  $T_{\text{B}}$  (fitted by *Duchamp*) and peak  $N_{\text{HI}}$  (measured from the column density map). However, small systematic errors in an order of 5–10% of derived values may also be present in these parameters. The *Duchamp* determined velocity FWHM values, however, are generally very accurate (see Figure 8 of Westmeier et al. 2011). We will compare our catalog with the catalog compiled from a recent study by Venzmer et al. (2012), hereafter V12, in Appendix.

### 3.1. Comparison with P02 Catalog

Here we compare our catalog to the P02 HVC catalog. The P02 catalog is based on HIPASS data, which have been reprocessed with the MINMED5 method to recover extended emission (Putman 2000). The catalog covers the entire sky in the declination range  $-90^\circ$  to  $+2^\circ$ , and the velocity range of  $+90 \text{ km s}^{-1} \lesssim |V_{\text{LSR}}| < +500 \text{ km s}^{-1}$ . The  $|V_{\text{LSR}}| < 90 \text{ km s}^{-1}$  limit does not exclude all emission associated with the Milky Way at low Galactic latitudes, and an additional constraint of deviation velocity was applied to their selection criterion. The search was performed via an automated friends-of-friends HVC finding algorithm of de Heij et al. (2002).

In Figure 5, we show a comparison between HVCs from the P02 catalog that fall within our searched GASS survey volume and in our catalog. The total number of identified HVCs in this region is 419 for our catalog and 448 for the P02 catalog. We point out that our catalog includes 30 clouds which straddle our velocity boundary at  $V_{\text{LSR}} = 150 \text{ km s}^{-1}$  and 71 clouds which extend over to the boundary of masked Milky Way emission region. About 230 HVCs are identified to be the same cloud in the two catalogs. The differences between the catalogs are due to: (a) degrees of breaking up or merging clouds in extended complexes, for which *Duchamp* tends to merge clouds while the friends-of-friends algorithm employed by P02 tends to break up clouds; (b) the superior brightness sensitivity of HIPASS compared to GASS (9 mK per  $15 \text{ km s}^{-1}$  compared with 15 mK per  $15 \text{ km s}^{-1}$  in GASS), resulting

in more faint sources to be detected in P02; (c) the excellent spectral resolution of GASS has allowed us to resolve narrow-line HVCs in the region, for which the spectral lines would have been smeared out in the case of coarser spectral resolution of HIPASS; (d) GASS has a better baseline coverage at the Galactic plane than HIPASS, resulting in more sources to be detected near the Galactic plane. We present a velocity FWHM distribution of both catalogs in Figure 6. HVCs that straddle our masked Milky Way emission boundaries and galaxies have been excluded in the plot. This figure shows that the majority of HVCs in the P02 catalog possesses larger velocity FWHM (30–35 km s<sup>-1</sup>) than ours (10–25 km s<sup>-1</sup>).

### 3.2. Completeness of the catalog

We adopted the same method as described in Begum et al. (2010) to evaluate the completeness of our catalog. Ten fake clouds with various input parameters were injected into our data cube at random locations. The injected fake clouds were modeled with the Gaussian function. Input parameters of LSR velocity, peak  $T_B$ , velocity FWHM, position angle, angular size in term of semi-major and semi-minor axes were randomly selected from various ranges. Ranges of input parameters were determined based on the cloud properties in our catalog.

We performed four sets of simulations with fake clouds being injected into the data cube between 150 km s<sup>-1</sup> and 450 km s<sup>-1</sup> LSR velocities:

- Bright clouds with a narrow velocity line width:  $T_B = 1.1\text{--}3.0$  K, velocity FWHM = 5–15 km s<sup>-1</sup>, semi-major axis = 0.3°–0.7°, semi-minor axis = 0.2°–0.4°.
- Bright clouds with a broad velocity line width:  $T_B = 1.1\text{--}3.0$  K, velocity FWHM = 16–30 km s<sup>-1</sup>, semi-major axis = 0.5°–1.0°, semi-minor axis = 0.2°–0.4°.
- Faint clouds with a narrow velocity line width:  $T_B = 0.14\text{--}1.0$  K, velocity FWHM = 5–15 km s<sup>-1</sup>, semi-major axis = 0.3°–0.7°, semi-minor axis = 0.2°–0.4°.
- Faint clouds with a broad velocity line width:  $T_B = 0.14\text{--}1.0$  K, velocity FWHM = 16–30 km s<sup>-1</sup>, semi-major axis = 0.3°–0.7°, semi-minor axis = 0.2°–0.4°.

Injected bright and faint clouds with a narrow velocity line width were fully recovered. The detection rates are 8/10 and 9/10 for faint and bright clouds with a broad velocity line width, respectively. The bright cloud with a broad velocity line width was missed because it was merged with another neighboring cloud. This is not uncommon considered that a cloud



with a broader velocity line width has a higher chance in overlapping with another cloud in a crowded region, and hence merged into a larger cloud complex. Faint clouds with a broad velocity line width can be lost in the background noise. To summarize, it is likely that our catalog missed faint, broad velocity line width clouds but *Duchamp* is relatively reliable in detecting narrow line width clouds for the studied region.

#### 4. General Distribution and Properties

The integrated HI column density map of HVCs in the region of the LA shows a significant concentration of HVCs between Galactic longitude  $240^\circ$  to  $260^\circ$  and Galactic latitude  $-30^\circ$  to  $+0^\circ$  (see Figure 1 and §6). This population appears to be clumpy but has a few larger, more complex clouds ( $\sim 3^\circ$ – $5^\circ$  in angular size). Velocity field maps in the LSR and GSR reference frames, as shown in Figures 7 and 8, indicate large velocity gradients for the LA I and LA II complexes. Faint or thin filamentary structures of complex clouds are not visible in these maps but can be seen in the moment maps of individual sources (e.g., see Figures 2 and 3). We assume all of these HVCs are originated from the MCs and are associated with the LA due to their close proximity on the sky to the MCs and their similar range of velocities. The following statistical analysis excludes galaxies and objects otherwise flagged in the catalog.

We present the kinematic distributions of HVCs in  $V_{LSR}$ ,  $V_{GSR}$  and  $V_{LGSR}$  versus Galactic longitude and latitude in Figures 9 and 10, respectively. A comparison between HVCs in the P02 catalog (black dots) and ours (red dots) is also shown. The main difference is that our catalog only includes sources with  $V_{LSR} > 150 \text{ km s}^{-1}$ . In the top panel of Figure 9 there are more positive than negative LSR velocity HVCs in the given Galactic longitude range. The overall velocity distribution of all P02 HVCs in Galactic and Local Group reference frames (middle and bottom panels of Figure 9) has nearly equal number of HVCs with positive and negative velocities. The HVCs in our catalog are evenly distributed across the Galactic longitude between  $240^\circ$  and  $320^\circ$  in all reference frames.

The kinematic distributions of our HVCs in Galactic latitude is slightly different than for the HVCs in the P02 catalog. The top panel of Figure 10 shows the lack of identified clouds in the range of  $150 \text{ km s}^{-1} < V_{LSR} < 190 \text{ km s}^{-1}$  and  $-15^\circ < b < +15^\circ$  in our catalog. The lack of clouds in this region is caused by the way we constructed the data cube by deliberately masking out most of the emission in this velocity range to avoid any contamination from the Galactic HI emission (see §2). There is a lack of clouds at higher Galactic latitude as the velocity increases in all reference frames.

In Figure 11, we show histograms of  $V_{LSR}$ ,  $V_{GSR}$ , Galactic longitude and latitude (from top to bottom panels). The median  $V_{LSR}$  and  $V_{GSR}$  for the HVCs in the catalog are  $232 \text{ km s}^{-1}$  and  $42 \text{ km s}^{-1}$ , respectively, which is consistent with the mean radial velocity of the LA (Brüns et al. 2005). We find that the number of clouds declines gradually as  $V_{LSR}$  increases above  $200 \text{ km s}^{-1}$ . Nearly the same number of clouds per  $5^\circ$  bin is found between Galactic longitude  $250^\circ$  and  $300^\circ$  (third panel). The total number of clouds below the Galactic plane outnumbers those above the Galactic plane, with a large fraction agglomerated between Galactic latitude  $-25^\circ$  and  $-10^\circ$  (bottom panel), where the region is closer to the LMC.

In Figure 12, we show the distribution function of peak H I column density, which can be described by a power law:  $f(N_{\text{HI}}) \propto N_{\text{HI}}^\alpha$ . The distribution shows that high column density clouds are rare. The turn-over at the low column density end of the distribution indicates that the population is limited by the survey sensitivity ( $1\sigma = 3.5 \times 10^{17} \text{ cm}^{-2}$ ). A linear function was fitted in the log–log space and a negative slope of  $-1.0$  was determined. This yields the final form of the distribution function as  $f(N_{\text{HI}}) \propto N_{\text{HI}}^{-2.0}$ . Comparing the distribution function of peak  $N_{\text{HI}}$  in the LA region with the MS (see Figure 10 of Putman et al. 2003), we find that both distributions turn-over simultaneously at the low column density end but the slope is steeper for their distribution function ( $\alpha = -2.8$ ). This implies that clouds of all H I masses in the MS contribute significantly to the total H I mass of the Magellanic System.

## 5. High-Velocity Cloud Morphological Classification

Different shapes of HVCs have been identified in the past, head-tail clouds in particular have been studied extensively (see e.g., Brüns et al. 2000; Westmeier et al. 2005; Putman et al. 2011). Examining the integrated H I column density and velocity field maps of each cloud, we can classify the HVCs into 5 groups: (1) clouds with head-tail structure and with velocity gradient (HT); (2) clouds with head-tail structure but without velocity gradient (:HT); (3) bow-shock shaped clouds (B); (4) symmetric clouds (S); and (5) irregular/complex clouds (IC). In Figure 13, we show different morphological type of clouds in our catalog. An analysis of groups 1–4 is given in the following subsections.

### 5.1. Head-Tail Clouds

Traditionally, a head-tail cloud is defined as a cloud which appears to be cometary with a compressed head trailed by a relatively diffuse tail; and a clear column density gradient is

visible (Brüns et al. 2000). In this study, we find that some head-tail clouds consist of an additional clump of diffuse gas or have a kink in the tail, slightly more complex than the traditional head-tail clouds. This structure suggests a fraction of the gas is being ripped off from the main condensation when it interacts with the surrounding halo gas.

Among the head-tail clouds, some show a velocity gradient, which is generally also associated with a column density gradient. Such a velocity gradient is another possible indicator for the detection of distortion caused by the interaction between clouds and an ambient medium (e.g., see PSM11; Brüns et al. 2000). Detection of a velocity gradient strongly depends on the spectral resolution of the data. Because of the high spectral resolution of GASS, in contrast to HIPASS, it is feasible to measure velocity gradient in addition to the HI column density gradient when classifying head-tail clouds. We divide the head-tail clouds into two types (group 1 & 2) and analyze them separately.

The total number of head-tail clouds is 100 ( $\sim 25\%$  of the sample), with typical head and tail column density different by a factor of 5 (typically  $\Delta N_{\text{HI}} \sim 4 \times 10^{18} \text{ cm}^{-2}$ ). 60% (61/100) of the head-tail clouds show a clear velocity gradient. A wide range of velocity differences between the head and tail ( $\sim 5\text{--}25 \text{ km s}^{-1}$ ) is detected. We find that this particular group of head-tail clouds with velocity gradient consists of two subgroups, with the velocity of the head either leading (pHT) or lagging (nHT) the tail. The number in the subgroups is about the same, 30 and 31, respectively.

In Figure 14, we show the peak HI column density distributions of head-tail clouds with velocity gradient (top panel) and without velocity gradient (bottom panel) in the region of the LA. The pointing direction of the head-tail clouds is also presented, with the head and tail having been enlarged for better visibility. As discussed in §3, the accuracy of the position angle is subject to the fitting methods and complexity of the cloud shape. To better represent the pointing direction of the clouds, we visually inspected each head-tail cloud and manually adjusted the Gaussian fit position angle whenever necessary.

The head-tail clouds appear to be pointing in a random direction regardless whether they belong to group 1 or group 2. In contrast, the study by PSM11 found that the majority of head-tail clouds in the region of the LA point in the general direction of the North Galactic Pole, consistent with the general motion of the Magellanic System. The different conclusions may partly be due to the differences in selection criteria: (a) the velocity gradient is not well measured in PSM11; (b) only compact, isolated HVCs (CHVCs) are searched for head-tail structure in PSM11; (c) the selection of head-tail clouds is a subjective process. We have about factor of two more head-tail clouds with velocity gradient than PSM11 in the same region. The implication of this random motion for the formation of the LA and its interaction with the Galactic halo will be discussed in §6.2.

Examining the peak HI column density distributions of both head-tail groups, we find that they populate the entire range of HI column densities and are spread over the entire region. The distribution in  $V_{LSR}$  for both groups is shown in Figures 15 and 16, in which a dichotomy is found above and below the Galactic plane. Above the Galactic plane, majority of the HT and :HT clouds possess  $V_{LSR} < 225 \text{ km s}^{-1}$ . Below the Galactic plane, it is populated by HT clouds with a wide range of  $V_{LSR}$ .

The distributions of peak HI column density and velocity FWHM of these two head-tail groups as compared to the general population of HVCs in this study are presented in Figure 17. The black, blue and red histograms represent all HVCs, head-tail clouds with velocity gradient (HT) and head-tail clouds without velocity gradient (:HT) clouds, respectively. The peak HI column density distributions are fairly similar in the cases of all HVCs and HT clouds, with the majority in the range of  $18.4 < \log(N_{\text{HI}}/\text{cm}^{-2}) < 18.6$  (top panel). This result is different from the recent study by PSM11, where the majority of head-tail clouds possess  $\log N_{\text{HI}} > 19.0$ . This is a factor of 2.5 higher in column density than those found in our sample. This is caused by the difference in the overall peak HI column density distribution and number of detected narrow line width clouds. The larger number of narrow velocity line width clouds in this study than P02 is not due to the false detections (see §3.2). *Duchamp* tends to merge clouds rather than breaking them into smaller clumps, which would result in a larger velocity line width for a merged cloud than smaller clumps. The peak HI column density distribution for :HT clouds is rather flat, most likely because of the small sample size. The velocity FWHM distributions are asymmetric with a peak at  $22 \text{ km s}^{-1}$  in all cases (bottom panel). Both velocity FWHM distributions of HT and :HT clouds extend out to  $\sim 40 \text{ km s}^{-1}$ .

To analyze the two subgroups of head-tail clouds with velocity gradient (i.e., pHT and nHT), we plot them with different symbols in Figure 18. The plus and square symbols represent the pHT and nHT clouds, respectively. There are approximately equal numbers of pHT clouds and nHT clouds above and below the Galactic plane for both the peak HI column density and  $V_{LSR}$  distributions. As for the distribution of  $V_{LSR}$  (bottom panel), pHT clouds possess slightly lower  $V_{LSR}$  ( $< 200 \text{ km s}^{-1}$ ) than nHT clouds ( $< 250 \text{ km s}^{-1}$ ) above the Galactic plane. Below the Galactic plane, pHT clouds are evenly distributed across the range of  $V_{LSR}$ , and nHT clouds dominate at  $V_{LSR} > 250 \text{ km s}^{-1}$ .

## 5.2. Symmetric and Bow-Shock Clouds

The bow-shock shaped cloud is characterized by a dense core with two deflected gas wings, which have lower column density than the core. The presence of this type of cloud

suggests ram-pressure interaction with the ambient medium. On the other hand, symmetric clouds do not exhibit any morphological signs of disturbance. We note, however, that a head-tail cloud aligned with the major axis along the line of sight would also appear as a symmetric cloud.

In Figure 19, we show the distributions of symmetric (diamonds) and bow-shock shaped (crosses) clouds in peak HI column density and  $V_{LSR}$ . There are only few high HI column density ( $> 10^{18} \text{ cm}^{-2}$ ) symmetric clouds are found above the Galactic plane. Otherwise, they cover a wide range of  $N_{\text{HI}}$  in the region of the LA. The majority of these clouds fall between  $225 \text{ km s}^{-1}$  and  $340 \text{ km s}^{-1}$  below the Galactic plane and less than  $250 \text{ km s}^{-1}$  above the Galactic plane. With a small sample of bow-shock shaped clouds, we conclude that the typical bow-shock shaped cloud has  $N_{\text{HI}} \sim 0.2 - 1 \times 10^{19} \text{ cm}^{-2}$  and velocity less than  $250 \text{ km s}^{-1}$ .

34% (23/69) of symmetric clouds also exhibit a velocity gradient. Velocity gradients in symmetric clouds can be caused by several effects. For example, there may be an angle between the HVC velocity vector and the line of sight; there could be rotation in the clouds; two or more HVCs are superimposed on the same line of sight (Brüns et al. 2000); and fluctuations in the background HI emission (Begum et al. 2010). There is no preferred direction of the velocity gradient for symmetric clouds in our catalog. We rule out projection of LSR velocity as the cause of velocity gradient. The typical velocity gradient is  $\sim 0.3\text{--}0.8 \text{ km s}^{-1} \text{ arcmin}^{-1}$ , which is similar to the range ( $0.5\text{--}1 \text{ km s}^{-1} \text{ arcmin}^{-1}$ ) found among the compact clouds studied by Begum et al. (2010). We note that our clouds are unresolved and thus subject to the effect of beam smearing.

## 6. Discussion

### 6.1. Implications of LA morphology for the origin of the LA

With the large sky coverage of GASS, we have uncovered new extended features of the Magellanic Leading Arm. In Figure 20, we show the relative position of the LA I, LA II and LA III (top figures) and individual LA complexes as identified by *Duchamp* (bottom subfigures). The red boxes highlight the extended features that were not detected in Brüns’ survey. The extended feature in LA I has been seen in other all-sky HVCs map (see e.g., Putman et al. 2002). It was not detected in the Brüns’ survey due to its longitude coverage cutoff at  $310^\circ$  near the LA I region.

The other extended feature seen in LA III is new. This feature consists of clumps connected by diffuse, low HI column density filaments. The most interesting part about this

extended feature is what appears to be a “bridge” connecting the LA II (see the arrow in top figure). The velocity map of this extended feature also shows similar velocity between LA II and LA III near the “bridge”. This implies that LA II and LA III might have been part of a larger cloud complex in the past and have been pulled apart.

Here we report a new population of clouds, named LA IV, that is located South of the Galactic plane and to the north-west of the LMC. Although LA IV has also recently been reported by V12, the defined boundary of LA IV is more extended in this study than V12 (see the schematic diagram of the LA IV feature at the top right panel of Figure 20). The median  $V_{LSR}$  of LA IV is  $\sim +260$  km s $^{-1}$ . The blue and dashed lines mark the estimated boundary and extended boundary of the population in the top left panel of Figure 20, respectively. The morphology of LA IV is different from its counterparts, the LA I, II and III complexes. It is formed by a stream of cloudlets rather than a large complex, which the majority of them are head-tail and symmetric clouds, and spanning  $\sim 50^\circ$  across the sky.

The origin of the LA is somewhat controversial. The overall velocity structure of the H I gas suggests that the LA originates from the LMC (Putman et al. 1998). The coincidence of the LA I position and morphology with the LMC southeast H I overdensity region further supports this observational evidence (Nidever et al. 2008). While metallicity measurements from HST spectra of background sources toward the MS and LA II only constraint their origin to the MCs ( $Z = 0.2 - 0.4$  solar; Lu et al. 1994, 1998; Gibson et al. 2000), new measurements of FUSE and HST spectra suggest that they originate from the SMC (Sembach et al. 2001; Fox et al. 2010). This observational evidence is supported by various simulations (see Connors et al. 2006; Diaz & Bekki 2011b).

If we ignore the controversy and assume that the LA has a single origin, it does not explain why the LA IV has a different morphology than its counterparts. A possible explanation is that the LA IV has a different origin. In fact, the stream of cloudlets that form the LA IV appears to trace back to the LMC (see Figure 20). This explanation would fit in the model scenario of SMC origin for the LA I, LA II and LA III. Nevertheless, measurement of metallicity using background sources toward the LA IV and future simulations that incorporate the LA IV are necessary.

Distance must have an effect on the morphology because the H I gas can interact with different ambient medium in different regions of the Galactic halo. With the exception of the LMC and SMC distances (50 and 60 kpc, respectively), distances to the LA and MS are hard to determine. According to the tidal models, the MS is further away from the Galactic plane than the MCs and the LA, with distances of 50–100 kpc at its tip (Yoshizawa & Noguchi 2003; Connors et al. 2006). An empirical study of filaments near the tip of the MS estimated a distance of 70 kpc, which is in agreement with the tidal mod-

els (Stanimirović et al. 2008). The LA is at an approximate kinematic distance of 21 kpc (McClure-Griffiths et al. 2008), based on the evidence of interaction between the LA I with the Galactic disk gas. This distance is smaller than the estimate due to cloud disruption timescale, in which the gas stream from the MCs is not expected to reach the disk in the form of HI clouds (Heitsch & Putman 2009). Simulations also put the distance of the LA to  $\sim 50$  kpc (see Figure 4 of Diaz & Bekki 2011b), although addition of ram-pressure stripping could result in a closer distance (Connors et al. 2006).

Examining the overall HI gaseous feature of the Magellanic System, we find that the global cloud morphology in the LA region is strikingly similar to the northern extension region of the MS (Nidever et al. 2008; Stanimirović et al. 2008). Both regions are rather clumpy and are populated with narrow line width clouds. These narrow line width clouds are generally exhibit multiphase structure, which consists of a cold core surrounded by a warm envelope. The existence of such multiphase HI clouds along the northern tip of the MS, which is at a distance of 80 kpc, is rather surprising (Stanimirović et al. 2008). Future physical properties study of individual compact HVCs along the northern extension of the MS is needed to answer this question.

## 6.2. Implications of head-tail clouds for the formation of the LA

The morphology of HVCs provides an important clue in studying the interaction between the neutral hydrogen gas and the ambient medium in the Galactic halo. Head-tail clouds are a classic example of cloud disruption via ram-pressure stripping when moving through the halo medium. They are relatively common as compared to the other morphological types. Such interaction commonly results in Kelvin-Helmholtz and thermal instabilities, and ultimately cloud fragmentation and evaporation (Konz et al. 2002).

Parameters such as the cloud size, halo and cloud densities have been shown to govern cloud stability in 3-dimensional hydrodynamical simulations (see e.g., Heitsch & Putman 2009; Quilis & Moore 2001; hereafter HP09 and QM01, respectively). In the QM01 models, pure gas and extragalactic dark-matter dominated HVCs with various gas densities, velocities and temperatures were investigated. They found that a tail with  $N_{\text{HI}} \geq 10^{19} \text{ cm}^{-2}$  appears when the external medium exceeds the density of  $10^{-4} \text{ cm}^{-3}$ , although a weak, faint tail with  $N_{\text{HI}} \sim 10^{18} \text{ cm}^{-2}$  also becomes visible when the density of the external medium reaches  $2 \times 10^{-5} \text{ cm}^{-3}$ . The setup of the HP09 simulations was slightly different from QM01. They took into account the heating by an ultraviolet radiation field and metallicity-based cooling mechanisms. Various halo density profiles, cloud masses and velocities were tested for their wind-tunnel and free-fall models. The wind-tunnel model is best described as exposing

the HVC to a wind with constant velocity and density. The free-fall model follows the trajectory of the HVC through an isothermal hydrostatic halo toward the disk. While both studies only consider clouds at lower  $z$  (within 10 kpc for the HP09 models), and hence might not be suitable to explain the formation and evolution of HVCs originating from the Magellanic Clouds, it is quite interesting to note that the simulations have successfully simulated prominent head-tail clouds even with kinks or multiple cores that are reminiscent of the observational structure of head-tail clouds in this study. The simulated timescale for the cloud disruption strongly depends on the physical conditions in the cloud and its interacting environment. Most head-tail clouds with high velocity are disrupted within 10 kpc and 100 Myr in the HP09 model but tail disruption can last as long as  $\sim 10^9$  yr in QM01 model after which the HI column density drops below the observational threshold.

The LA complexes are similar to head-tail clouds on a large scale. The directionality of their head and tail suggests that they are moving toward higher Galactic latitudes, although the curvature of LA II and LA III are in the opposite direction to LA I. The velocity gradient shows that the velocity at the head is slower than the tail in LA I and II (see Figure 7). This kind of velocity gradient is expected when the head of the cloud is decelerated while moving through the ambient medium.

Assuming that all small HVCs in the region of the LA (excluding cloudlets that form part of the LA IV) are fragments from the LA complexes due to cloud disruption, the directionality of the head-tail clouds should follow the direction of motion of the LA. However, this is not what we observed either for the head-tail clouds with or without velocity gradient (as mentioned in §5.1; see also Figure 14). The pointing direction of the head-tail clouds is random which suggests that turbulence in the medium must be at play. According to Audit & Hennebelle (2005), this scenario can be generated when the incoming warm neutral gas collides with the hotter ambient medium and creates a thermally unstable region. If the flow is weakly turbulent, part of the warm gas condenses into cold gas, and any thermally unstable cold gas will continue to fragment until thermal equilibrium is achieved. In the case of a strongly turbulent incoming flow, which is the case for the interaction between the LA and the Milky Way halo medium (based on the velocity of the gas stream), the fragmented clouds should appear distorted and irregular. Strong turbulence also promotes the occurrence of fragmentation for the thermally unstable clouds, and subsequently, more small, cold clouds with lower density. This scenario appears to agree with the properties of HVCs in the region of the LA.

In §5.1, we presented the dichotomy in radial velocity for the head-tail and symmetric HVCs above and below the Galactic plane (see Figures 15 and 19), in which the HVCs below the Galactic plane possess lower  $V_{LSR}$  than above the Galactic plane. Such dichotomy (or



gradient as a function of Galactic latitude) is also seen in simulations, although the gradient has an offset between the model and the observational data (see Figure 7 of Diaz & Bekki 2011b). Simulations only include gravitational force, we suggest that an orbital effect is the cause of such dichotomy. Since we are only interested in the real distortion due to interaction of the cloud with the ambient medium, we will only consider the head-tail clouds with velocity gradient for the rest of this discussion.

If we assume that all LA HVCs are traveling along the same orbit as the MC’s, we can use knowledge of the MC’s total velocity and vector components to estimate the tangential velocity ( $V_t$ ) of the HVCs from their measured radial velocities in the GSR frame. Hence, we can translate the median  $V_{GSR}$  of HT clouds above and below the Galactic plane into their associated tangential velocities ( $V_t$ ) based on the relative fractions of  $V_t$  and  $V_{GSR}$  of the MCs (LMC:  $V_t = 367 \text{ km s}^{-1}$ ,  $V_{GSR} = 89 \text{ km s}^{-1}$ ; SMC:  $V_t = 301 \text{ km s}^{-1}$ ,  $V_{GSR} = 23 \text{ km s}^{-1}$ ; Kallivayalil et al. 2006a). With the median  $V_{GSR}$  of  $-7$  and  $54 \text{ km s}^{-1}$  for clouds above and below the Galactic plane, the estimated tangential velocities are  $270 \text{ km s}^{-1}$  and  $330 \text{ km s}^{-1}$ , respectively. While the  $V_t$  difference is small, we can estimate the mean density of the halo region ( $n_h(z)$ ) that the clouds move through,

$$C_D f_c n_h(z) = \frac{2N_{HI}g(z)}{v^2} \quad (1)$$

(Benjamin & Danly 1997), where  $C_D$  is the drag coefficient,  $f_c = N_{HI}/(N_{HI} + N_{HII})$  is cloud neutral fraction,  $g(z)$  is the gravitational acceleration,  $N_{HI}$  is the total H I column density of the cloud and the  $v$  is velocity of cloud. We assume that the total H I column density of a typical head-tail cloud is  $10^{19} \text{ cm}^{-2}$ , the drag coefficient and cloud neutral fraction are 1.0, and the gravitational acceleration is constant ( $0.2 \times 10^{-8} \text{ cm s}^{-2}$ ) beyond 10 kpc (Wolfire et al. 1995) for determining the mean halo densities. For the velocities above and below the Galactic plane of  $270 \text{ km s}^{-1}$  and  $330 \text{ km s}^{-1}$ , we obtain  $n_h = 5.4 \times 10^{-5}$  and  $3.7 \times 10^{-5} \text{ cm}^{-3}$ , respectively. We note that the calculation is sensitive to the adopted cloud H I column density and uncertainty on  $f_c$ . Nevertheless, while the halo density is poorly known beyond 10 kpc, this exercise demonstrates that a slight difference in the halo density might cause the morphological differences between the LA I and LA II+LA III.

The presence of a large number of head-tail clouds in the region of the LA as compared to the MS is somewhat curious (see PSM11). High angular resolution study of filaments near the northern tip of the MS has also shown the dominance of spherical clouds and an absence of elongated or head-tail clouds (Stanimirović et al. 2008). Assuming an isothermal halo,  $P_{\text{ram}} \propto \rho v^2$ , where  $\rho$  is halo density and is proportional to  $d^{-2}$ , the distances predicted from the Diaz & Bekki (2011b) simulations would suggest a higher ram-pressure interaction for the LA than the bulk of MS. Both observational evidence and theory support ram-pressure stripping as a more important factor than gravitational force for producing the morphological

features of the LA. The inclusion of ram-pressure stripping in models could therefore result in closer predicted distances for the LA clouds, as suggested by the observational data. Finally, with the close distance of the LA, we suggest that fragmentation is not the only mechanism that produces the small clouds in the region. The cloud fragments with lower  $z$ -distances would experience increased background pressure which would increase the cooling rate. This would result in reforming of cold H I clouds, as seen under the free-fall model of HP09.

## 7. Summary and Conclusions

We have produced a catalog of high velocity clouds in the region of the Magellanic Leading Arm from Parkes Galactic All-Sky Survey data, using the cloud search algorithm *Duchamp*. We used *Duchamp* to parametrize cloud properties including position, velocity and velocity FWHM. We determined the angular size of sources via 2-dimensional Gaussian fitting and peak H I column density via searching the brightest pixel in the integrated maps. Comparison between our HVC catalog with that of Putman et al. (2002) in the same region and velocity range shows that the high spectral resolution of GASS allows us to recover clouds with narrow line widths. The total number of detected HVCs is 448 for P02 catalog and 419 for our catalog. The combined catalog contains  $\sim 625$  unique clouds.

We have presented the general distribution of HVCs in the catalog. The kinematic distributions with respect to Galactic longitude and latitude are generally consistent with the findings in P02. A trend of decreasing number of clouds from higher to lower Galactic latitude as velocity increases in all velocity reference frames was found. A morphological classification of clouds was presented, and distributions of each type were discussed.

An extended feature in the LA I complex that was not covered in the detailed study of the Magellanic System by Brüns et al. (2005) was noted. A new population of clouds that forms the LA IV and an extended feature that forms a diffuse “bridge” connecting the LA II and III complexes were also discovered. The discovery of the LA III extended feature demonstrates the importance of brightness temperature sensitivity and spectral resolution for an all-sky survey. Simulations have yet to reproduce this feature of LA.

The most significant result in this study was the detection of a large number of head-tail clouds in the region of the LA as compared to the MS, suggesting that ram-pressure stripping is relatively more important than gravitational forces for the morphology and formation of the LA. The LA I and II themselves are large head-tail clouds, which are moving toward higher Galactic latitudes and both show a large velocity gradient, with the head being lower than the tail. We found that there was no preferred pointing direction for the small

head-tail clouds. This suggests a scenario where the clouds are produced in a turbulent flow where incoming warm neutral gas collides with the hot halo ISM. The cloud morphologies are strongly correlated to the degree of turbulence in the ISM. The presence of strong turbulence is probably the cause for the observed morphologies and properties of clouds in the region.

A dichotomy in velocity for the head-tail and symmetric HVCs above and below the Galactic plane was found. Since such dichotomy is also seen in simulations of Diaz & Bekki (2011b), we suggest that an orbital effect is the cause. Finally, using the typical HI column density of cloud and tangential velocities above and below the Galactic plane, we infer a small difference in halo density. This suggests that the LA II and LA II+LA III are interacting with different halo environments, which might explain the morphological difference between them.

## A. APPENDIX: COMPARISON WITH V12 CATALOG

While this paper was under review, a similar study appeared in press by Venzmer et al. (2012). Here we compare our catalog to the V12 catalog, which was compiled using a similar studied area to this paper. Venzmer et al. (2012) extracted the GASS data cube from  $52 \text{ km s}^{-1}$  to  $400 \text{ km s}^{-1}$   $V_{LSR}$  and performed the source finding and parametrization with the image processing software, *ImageJ*. We refer the reader to V12 for a detailed description of source selection criteria. In Figure 21, we show a comparison between HVCs from the V12 catalog that fall within our studied area. The total identified HVCs in this region is 419 (our catalog) vs 433 (V12). Sixteen of HVCs in V12 catalog lie outside our studied area.

While the total number of clouds between the two catalog is similar, only  $\sim 120$  HVCs are identified to be the same cloud in the two catalogs. The differences are due to: (a) degrees of breaking up or merging clouds in extended complexes; (b) the searched velocity range; and (c) selection criteria for clouds. The degrees of breaking up or merging clouds can be easily seen in Figure 21 (e.g., near the region of LA I), which *ImageJ* breaks up more clouds than *Duchamp* for a given region. There are pros and cons for both source finding softwares in term of degrees of breaking up or merging clouds. The advantage of breaking up a large cloud complex into smaller sub-clouds allows analysis of individual sub-clouds (e.g., breaking up the LA I into LA 1.1–1.3). However, a high degree of breaking-up of clouds can result in missed detections such as the diffuse bridge-like feature we see connecting LA II and LA III.

As mentioned in §2, the Galactic HI emission is extremely strong in the velocity range

$0 \text{ km s}^{-1} \leq V_{LSR} < 150 \text{ km s}^{-1}$ . Mild contamination is also evident between 150 and  $190 \text{ km s}^{-1}$ . Part of the searched velocity range in V12 and this study are affected by Galactic HI emission. While we manually masked out the affected region, V12 applied a cut off to the velocity FWHM that excludes the Galactic HI emission. A comparison of velocity FWHM distributions in both catalogs in Figure 22 reveals a poor correlation. About 50% of clouds in V12 catalog have narrow line widths (defined here as velocity FWHM less than  $10 \text{ km s}^{-1}$ ). Close examination of a subset of the V12 narrow line width HVCs shows that some are real detection of small clumps, but some are false detections due to artifacts and noise peaks. Furthermore, there are a significant number of clouds with quoted velocity width much lower than we measure - in some cases as low as the GASS velocity resolution.

We compare the velocity FWHM and peak  $N_{\text{HI}}$  values of HVCs that are found in both catalogs. HVCs identified as the same source in the two catalogs, but without listed parameters in our catalog, are excluded from the comparison. Figures 23 and 24 show the comparison of the measurements (top panels) and the difference in measurements (bottom panels). We find  $\langle \Delta V_{\text{FWHM}} \rangle = -8.3 \text{ km s}^{-1}$ ,  $\sigma = 9.4 \text{ km s}^{-1}$ , 85 HVCs; the velocity FWHM measured in V12 is systematically lower than ours. The difference is more significant for broad line width HVCs ( $>20 \text{ km s}^{-1}$ ). Direct comparison for the velocity FWHM of other small clumps as detected in V12 cannot be made because they have been merged into larger clouds by *Duchamp*. Nevertheless, examining some of these HVCs in the GASS data cube, we find that the measurements in V12 are consistently underestimated. For peak  $N_{\text{HI}}$ , we find  $\langle \Delta N_{\text{HI}} \rangle = -0.25 \times 10^{19} \text{ cm}^{-2}$ ,  $\sigma = 0.91 \times 10^{19} \text{ km s}^{-1}$ , 85 HVCs. The peak  $N_{\text{HI}}$  measurements in V12 is also systematically lower than ours and with large differences for some of the HVCs.

BQF is the recipient of a John Stocker Postdoctoral Fellowship from the Science and Industry Research Fund. This research made use of APLpy, an open-source plotting package for Python hosted at <http://aplpy.github.com> and data from the Parkes Galactic All-Sky Survey. The Parkes radio telescope is part of the Australia Telescope National Facility which is funded by the Commonwealth of Australia for operation as a National Facility managed by CSIRO. We thank Tobias Westmeier for providing his parametrization algorithm and helpful comments; Matthew Whiting for providing helps on running *Duchamp*; Kenji Bekki for generating a fruitful discussion and the anonymous referee for his/her comments to help improving the original manuscript.

## REFERENCES

- Audit, E. & Hennebelle, P. 2005, *A&A*, 433, 1
- Barnes, D. G., Staveley-Smith, L., de Blok, W. J. G., & et al. 2001, *MNRAS*, 322, 486
- Begum, A., Stanimirović, S., Peek, J. E., Ballering, N. P., Heiles, C., Douglas, K. A., Putman, M., Gibson, S. J., Grcevich, J., Korpela, E. J., Lee, M.-Y., Saul, D., & Gallagher, III, J. S. 2010, *ApJ*, 722, 395
- Benjamin, R. A. & Danly, L. 1997, *ApJ*, 481, 764
- Besla, G., Kallivayalil, N., Hernquist, L., Robertson, B., Cox, T. J., van der Marel, R. P., & Alcock, C. 2007, *ApJ*, 668, 949
- Blaauw, A. & Tolbert, C. R. 1966, *BAN*, 18, 405
- Blitz, L., Spergel, D. N., Teuben, P. J., Hartmann, D., & Burton, W. B. 1999, *ApJ*, 514, 818
- Braun, R. & Burton, W. B. 1999, *A&A*, 341, 437
- Brüns, C., Kerp, J., Kalberla, P. M. W., & Mebold, U. 2000, *A&A*, 357, 120
- Brüns, C., Kerp, J., Staveley-Smith, L., Mebold, U., Putman, M. E., Haynes, R. F., Kalberla, P. M. W., Muller, E., & Filipovic, M. D. 2005, *A&A*, 432, 45
- Connors, T. W., Kawata, D., & Gibson, B. K. 2006, *MNRAS*, 371, 108
- de Avellez, M. A. 2000, *Ap&SS*, 272, 23
- de Heij, V., Braun, R., & Burton, W. B. 2002, *A&A*, 391, 159
- Diaz, J. & Bekki, K. 2011a, *MNRAS*, 413, 2015
- Diaz, J. D. & Bekki, K. 2011b, *ArXiv e-prints*
- Fox, A. J., Wakker, B. P., Smoker, J. V., Richter, P., Savage, B. D., & Sembach, K. R. 2010, *ApJ*, 718, 1046
- Gibson, B. K., Giroux, M. L., Penton, S. V., Putman, M. E., Stocke, J. T., & Shull, J. M. 2000, *AJ*, 120, 1830
- Heitsch, F. & Putman, M. E. 2009, *ApJ*, 698, 1485
- Houck, J. C. & Bregman, J. N. 1990, *ApJ*, 352, 506

- Kalberla, P. M. W., Burton, W. B., Hartmann, D., Arnal, E. M., Bajaja, E., Morras, R., & Pöppel, W. G. L. 2005, *A&A*, 440, 775
- Kalberla, P. M. W., McClure-Griffiths, N. M., Pisano, D. J., Calabretta, M. R., Ford, H. A., Lockman, F. J., Staveley-Smith, L., Kerp, J., Winkel, B., Murphy, T., & Newton-McGee, K. 2010, *A&A*, 521, A17
- Kallivayalil, N., van der Marel, R. P., & Alcock, C. 2006a, *ApJ*, 652, 1213
- Kallivayalil, N., van der Marel, R. P., Alcock, C., Axelrod, T., Cook, K. H., Drake, A. J., & Geha, M. 2006b, *ApJ*, 638, 772
- Kerton, C. R., Brunt, C. M., Jones, C. E., & Basu, S. 2003, *A&A*, 411, 149
- Konz, C., Brüns, C., & Birk, G. T. 2002, *A&A*, 391, 713
- Lu, L., Sargent, W. L. W., Savage, B. D., Wakker, B. P., Sembach, K. R., & Oosterloo, T. A. 1998, *AJ*, 115, 162
- Lu, L., Savage, B. D., & Sembach, K. R. 1994, *ApJ*, 437, L119
- Mastropietro, C., Moore, B., Mayer, L., Wadsley, J., & Stadel, J. 2005, *MNRAS*, 363, 509
- Mathewson, D. S., Cleary, M. N., & Murray, J. D. 1974, *ApJ*, 190, 291
- McClure-Griffiths, N. M., Pisano, D. J., Calabretta, M. R., Ford, H. A., Lockman, F. J., Staveley-Smith, L., Kalberla, P. M. W., Bailin, J., Dedes, L., Janowiecki, S., Gibson, B. K., Murphy, T., Nakanishi, H., & Newton-McGee, K. 2009, *ApJS*, 181, 398
- McClure-Griffiths, N. M., Staveley-Smith, L., Lockman, F. J., Calabretta, M. R., Ford, H. A., Kalberla, P. M. W., Murphy, T., Nakanishi, H., & Pisano, D. J. 2008, *ApJ*, 673, L143
- Muller, C. A., Oort, J. H., & Raimond, E. 1963, *Academie des Sciences Paris Comptes Rendus*, 257, 1661
- Münch, G. & Zirin, H. 1961, *ApJ*, 133, 11
- Nidever, D. L., Majewski, S. R., & Burton, W. B. 2008, *ApJ*, 679, 432
- Nidever, D. L., Majewski, S. R., Butler Burton, W., & Nigra, L. 2010, *ApJ*, 723, 1618
- Oort, J. H. 1966, *Bull. Astron. Inst. Netherlands*, 18, 421
- Putman, M. E. 2000, *PASA*, 17, 1

- Putman, M. E., de Heij, V., Staveley-Smith, L., Braun, R., Freeman, K. C., Gibson, B. K., Burton, W. B., Barnes, D. G., Banks, G. D., Bhathal, R., de Blok, W. J. G., Boyce, P. J., Disney, M. J., Drinkwater, M. J., Ekers, R. D., Henning, P. A., Jerjen, H., Kilborn, V. A., Knezek, P. M., Koribalski, B., Malin, D. F., Marquarding, M., Minchin, R. F., Mould, J. R., Oosterloo, T., Price, R. M., Ryder, S. D., Sadler, E. M., Stewart, I., Stootman, F., Webster, R. L., & Wright, A. E. 2002, *AJ*, 123, 873
- Putman, M. E., Gibson, B. K., Staveley-Smith, L., Banks, G., Barnes, D. G., Bhatal, R., Disney, M. J., Ekers, R. D., Freeman, K. C., Haynes, R. F., Henning, P., Jerjen, H., Kilborn, V., Koribalski, B., Knezek, P., Malin, D. F., Mould, J. R., Oosterloo, T., Price, R. M., Ryder, S. D., Sadler, E. M., Stewart, I., Stootman, F., Vaile, R. A., Webster, R. L., & Wright, A. E. 1998, *Nature*, 394, 752
- Putman, M. E., Saul, D. R., & Mets, E. 2011, *MNRAS*, 418, 1575
- Putman, M. E., Staveley-Smith, L., Freeman, K. C., Gibson, B. K., & Barnes, D. G. 2003, *ApJ*, 586, 170
- Quilis, V. & Moore, B. 2001, *ApJ*, 555, L95
- Reid, M. J. & Brunthaler, A. 2004, *ApJ*, 616, 872
- Sembach, K. R., Howk, J. C., Savage, B. D., & Shull, J. M. 2001, *AJ*, 121, 992
- Shattow, G. & Loeb, A. 2009, *MNRAS*, 392, L21
- Stanimirović, S., Hoffman, S., Heiles, C., Douglas, K. A., Putman, M., & Peek, J. E. G. 2008, *ApJ*, 680, 276
- Starck, J.-L. & Murtagh, F. 1994, *A&A*, 288, 342
- Venzmer, M. S., Kerp, J., & Kalberla, P. M. W. 2012, *A&A*, 547, A12
- Wakker, B. P. 1991, *A&A*, 250, 499
- Wakker, B. P. & van Woerden, H. 1991, *A&A*, 250, 509
- Westmeier, T., Brüns, C., & Kerp, J. 2005, *A&A*, 432, 937
- Westmeier, T., Popping, A., & Serra, P. 2011, *ArXiv e-prints*
- Whiting, M. T. 2012, *ArXiv e-prints*
- Williams, J. P., de Geus, E. J., & Blitz, L. 1994, *ApJ*, 428, 693

Wolfire, M. G., McKee, C. F., Hollenbach, D., & Tielens, A. G. G. M. 1995, *ApJ*, 453, 673

Yoshizawa, A. M. & Noguchi, M. 2003, *MNRAS*, 339, 1135



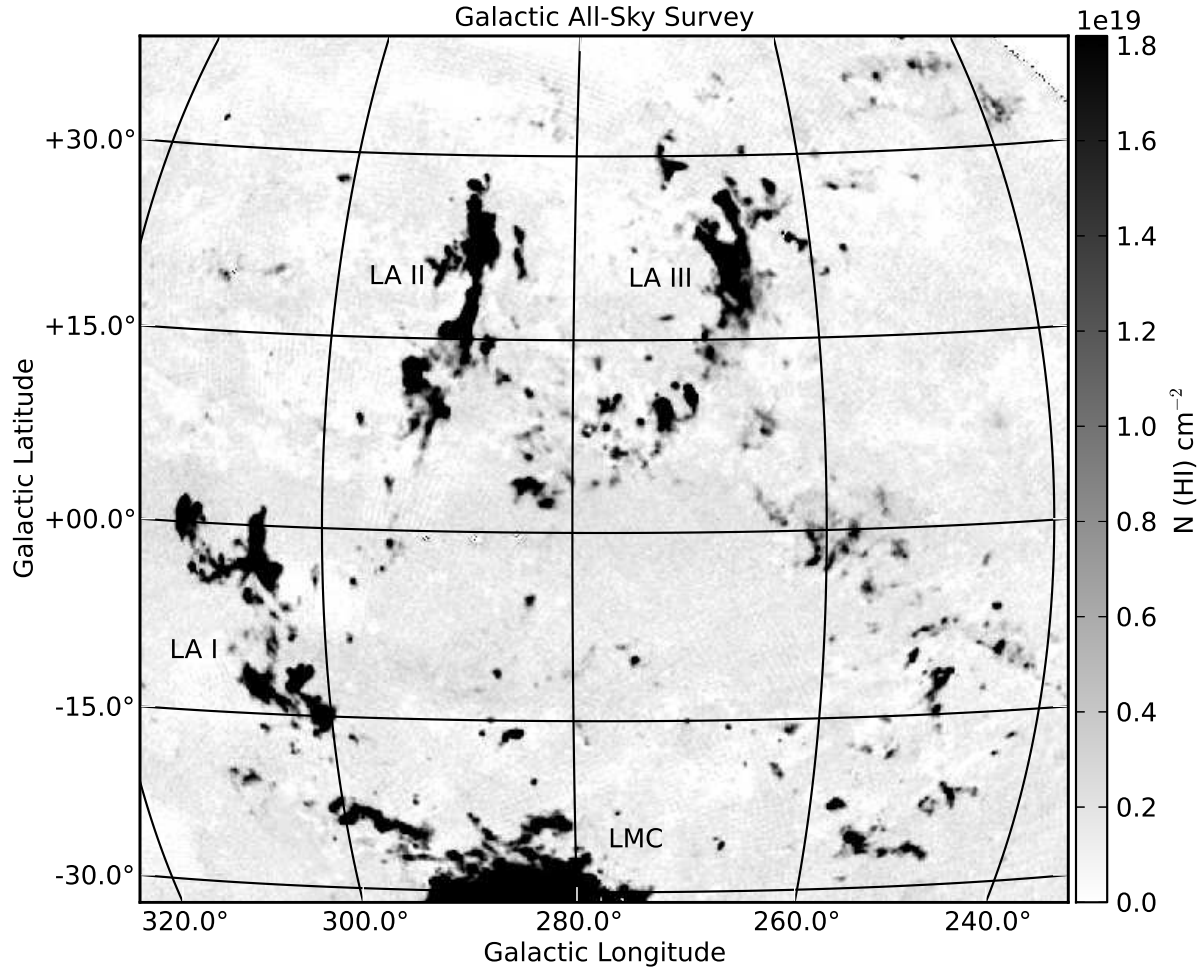


Fig. 1.— The integrated HI column density map of GASS in the region of the Magellanic Leading Arm. The HI column density scale is  $0$  to  $1.8 \times 10^{19} \text{ cm}^{-2}$ . Locations of the Leading Arm complexes I, II, III and the Large Magellanic Cloud are labeled.

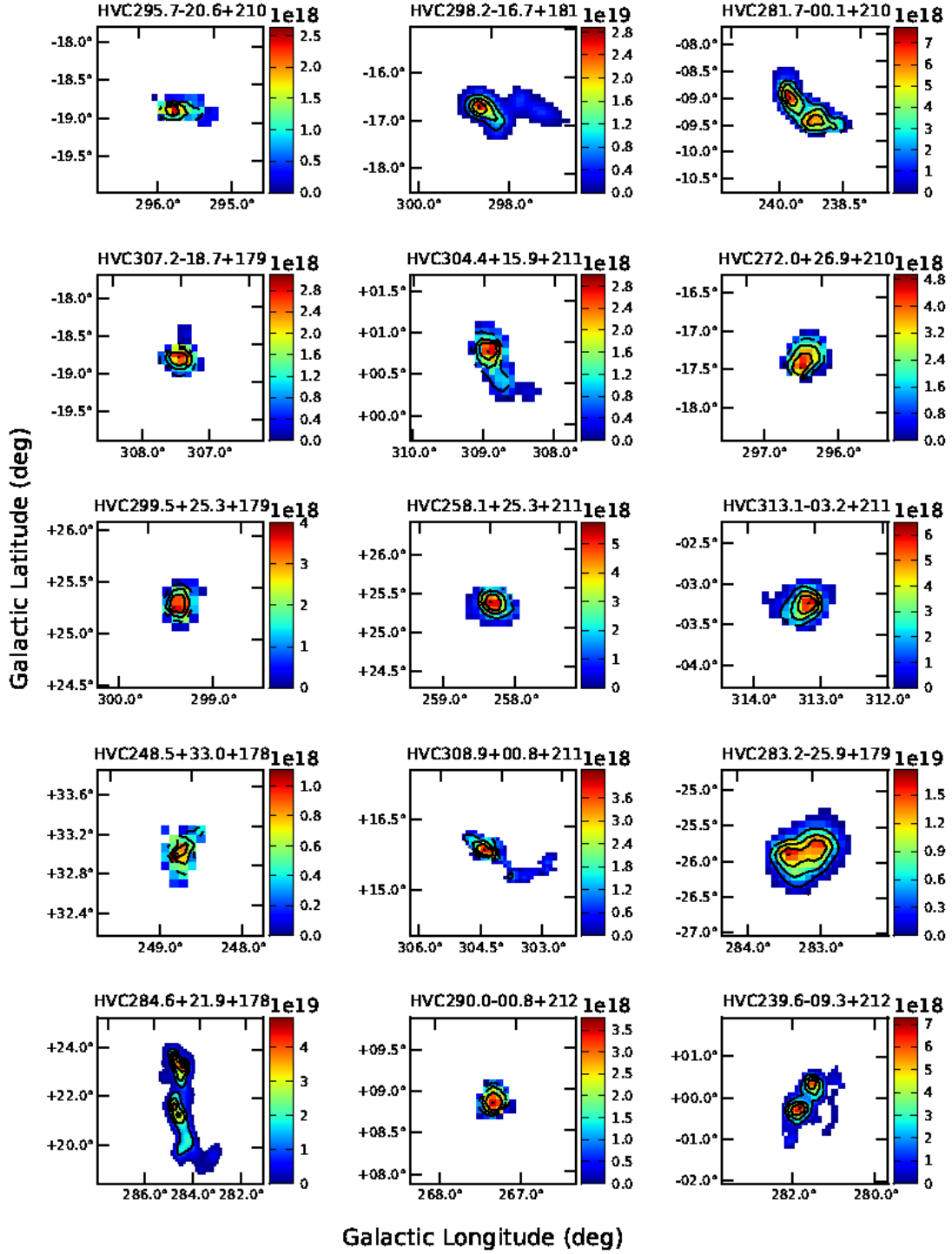


Fig. 2.— Examples of integrated HI column density maps of individual sources. Contours and colors representing the HI column density scale are shown.

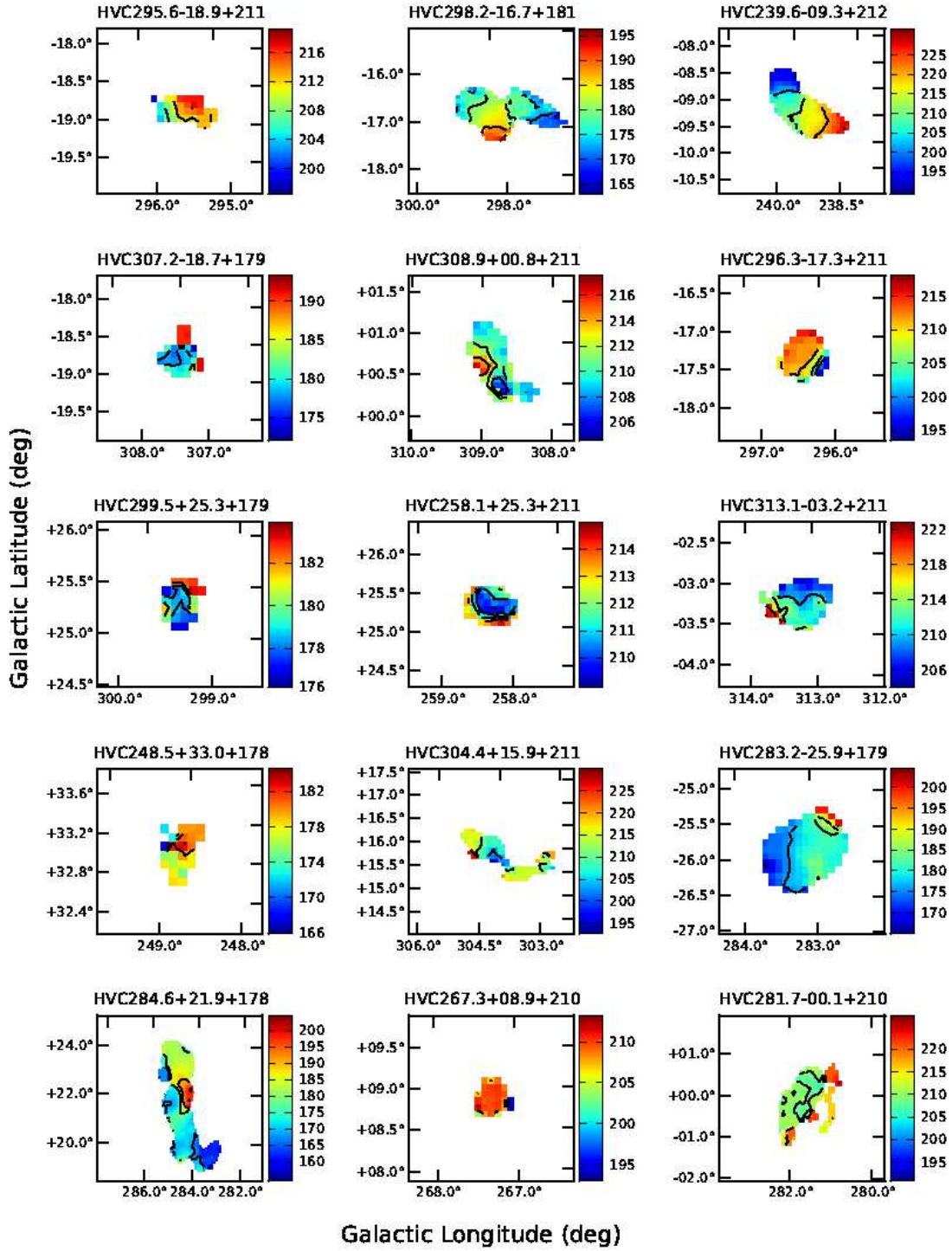


Fig. 3.— Examples of velocity field maps of individual sources. Contours and colors representing the LSR velocity are shown.

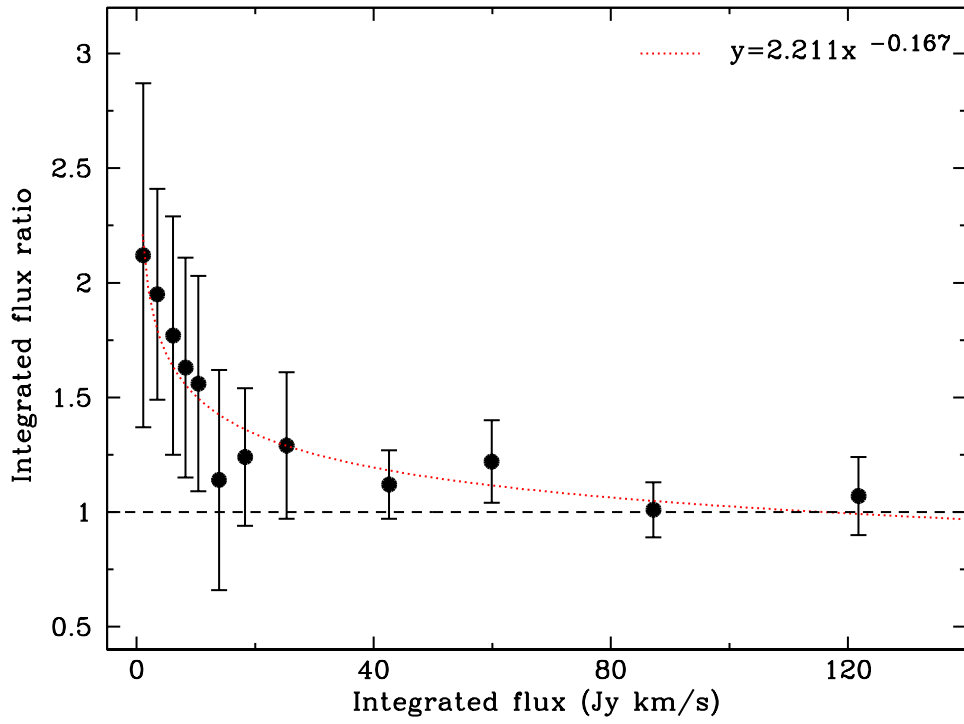


Fig. 4.— Ratio of “true” integrated flux ( $F_{\text{int}}$ ) to the integrated flux ( $F'_{\text{int}}$ ) measured by *Duchamp* as a function  $F'_{\text{int}}$ . The red dotted line is the fit to the data points, which represents our estimated correction to the *Duchamp* values.

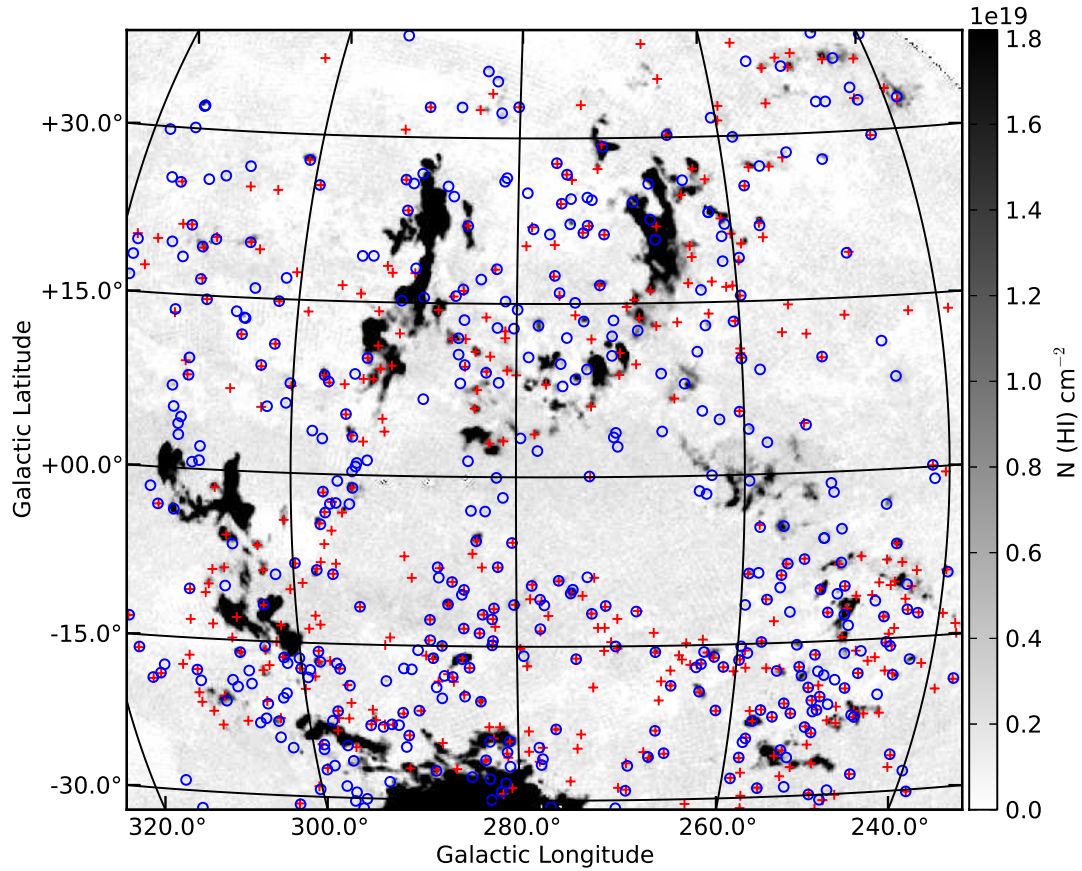


Fig. 5.— On-sky distribution of the 431 sources detected by *Duchamp* (blue circles) and the 448 sources detected by Putman et al. (2002) (red pluses) in the region of the Leading Arm. The integrated HI column density map of Figure 1 is shown. The sources from Putman et al. (2002) are within the same velocity range as the catalog presented in this paper. Comparison between the two catalogs is discussed in §3.1.

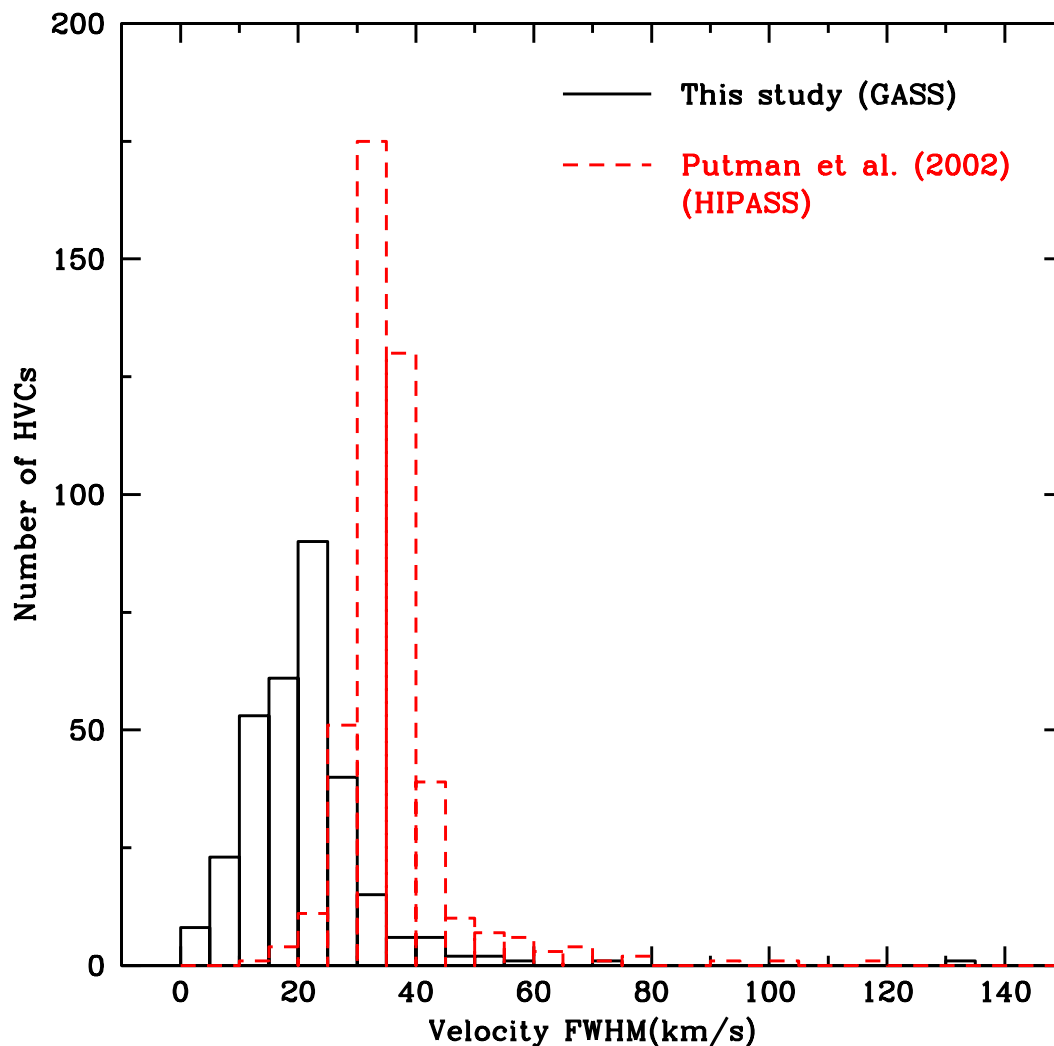


Fig. 6.— Histograms of velocity FWHM of HVCs in P02 (dashed line) and this study (solid line). Excluded from the plot are: 30 clouds that extend below  $V_{LSR} = 150 \text{ km s}^{-1}$ ; 71 clouds that extend into the masked Milky Way emission boundary; 10 clouds that extend into the spatial edge of the image and galaxies. A larger number of narrow-line width HVCs are recovered in this study as compared to P02. The difference is mainly due to the higher spectral resolution of GASS.

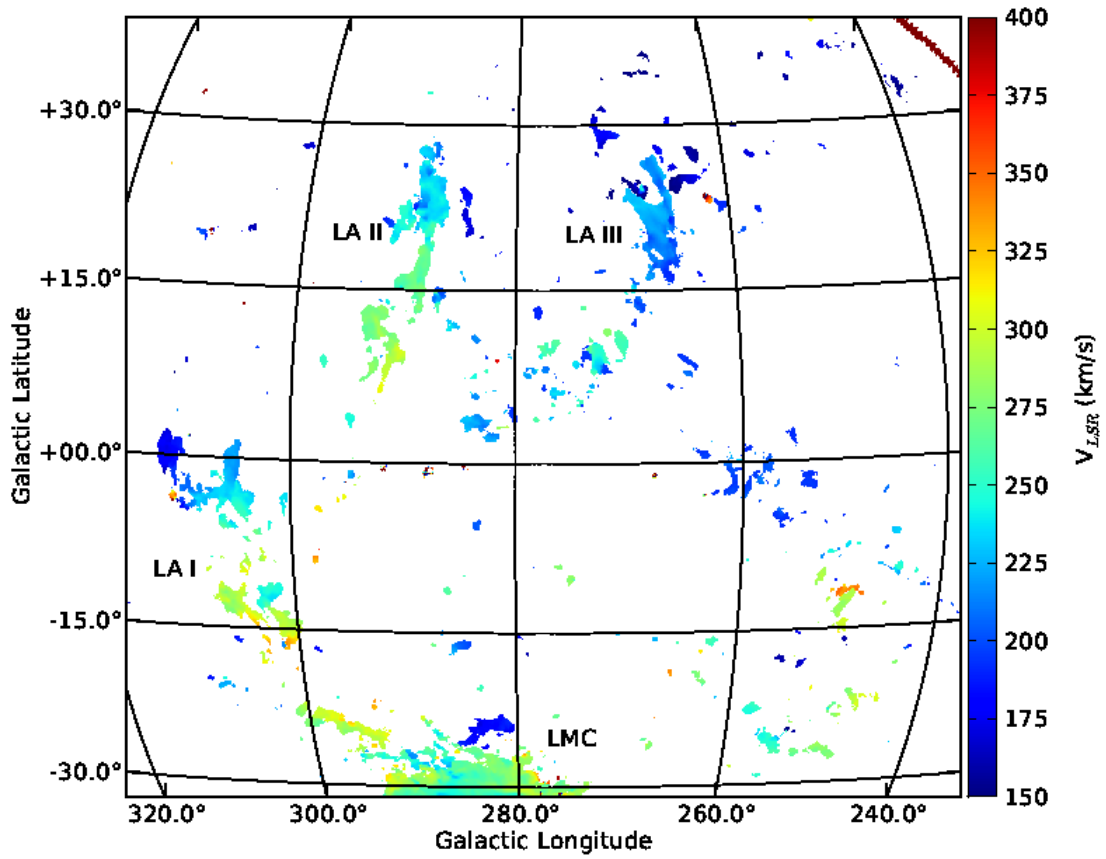


Fig. 7.— The velocity field map (first moment map) in the LSR velocity reference frame. The color bar represents the velocity range from 150 to 400 km s<sup>-1</sup>. The Leading Arm complexes and Large Magellanic Cloud are labeled.

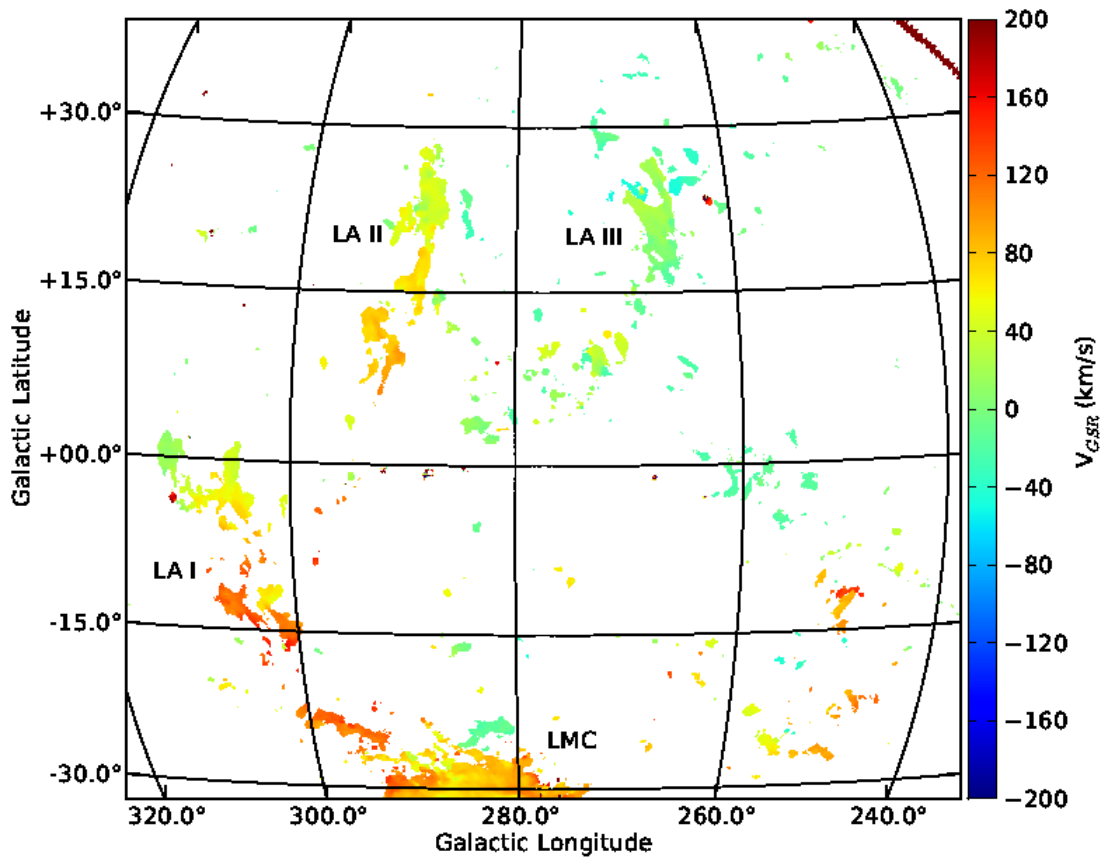


Fig. 8.— Same as Figure 7, except in the GSR velocity reference frame with a velocity range of  $-200$  to  $+200$   $\text{km s}^{-1}$ .



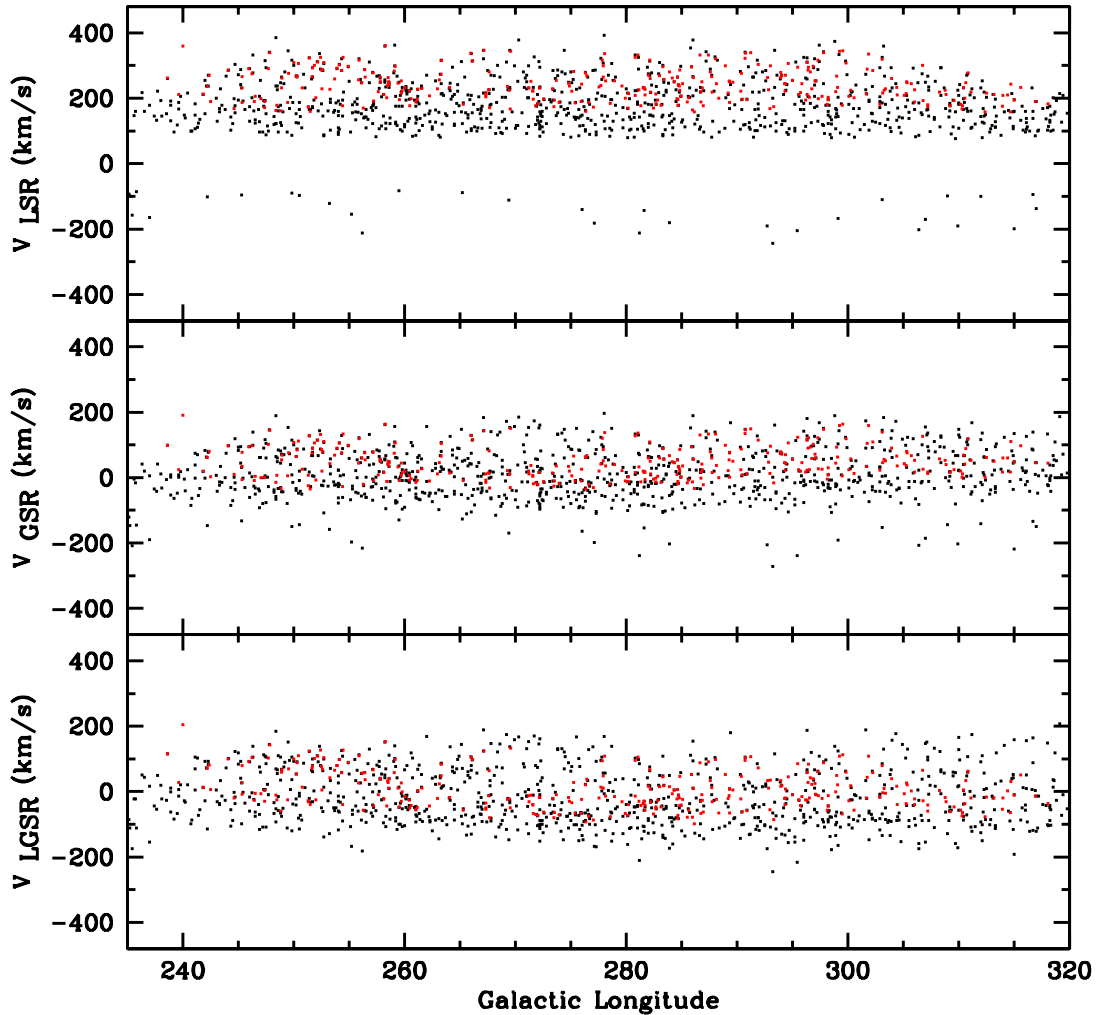


Fig. 9.— Kinematic distributions of HVCs in the  $V_{LSR}$ ,  $V_{GSR}$  and  $V_{LGSR}$  reference frames versus Galactic longitude (from top to bottom). The black and red dots represent HVCs in P02 and our catalog, respectively. Excluded from the plot are: 30 clouds that extend below  $V_{LSR} = 150 \text{ km s}^{-1}$ ; 71 clouds that extend into the masked Milky Way emission boundary; 10 clouds that extend into the spatial edge of the image and galaxies.

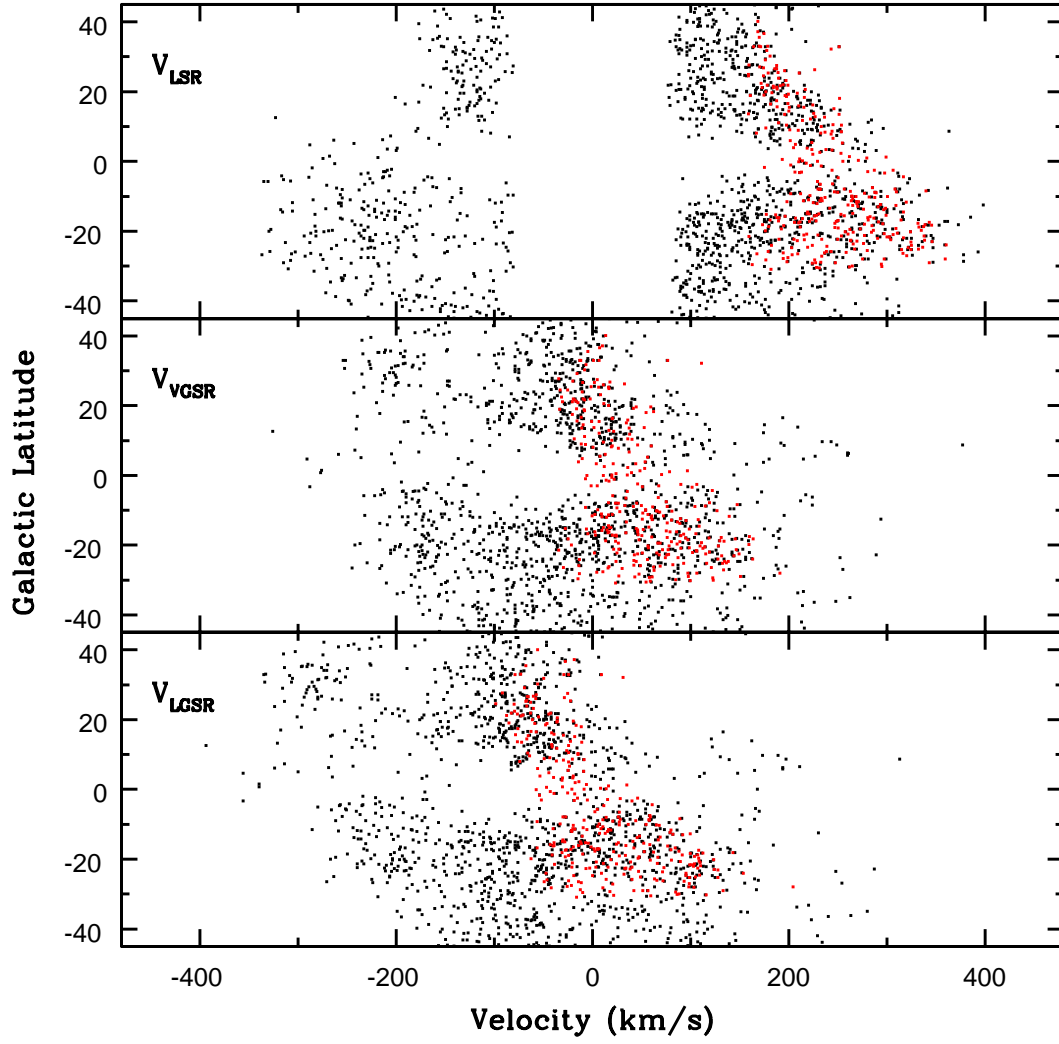


Fig. 10.— Same as Figure 9, except showing velocities versus Galactic latitude.

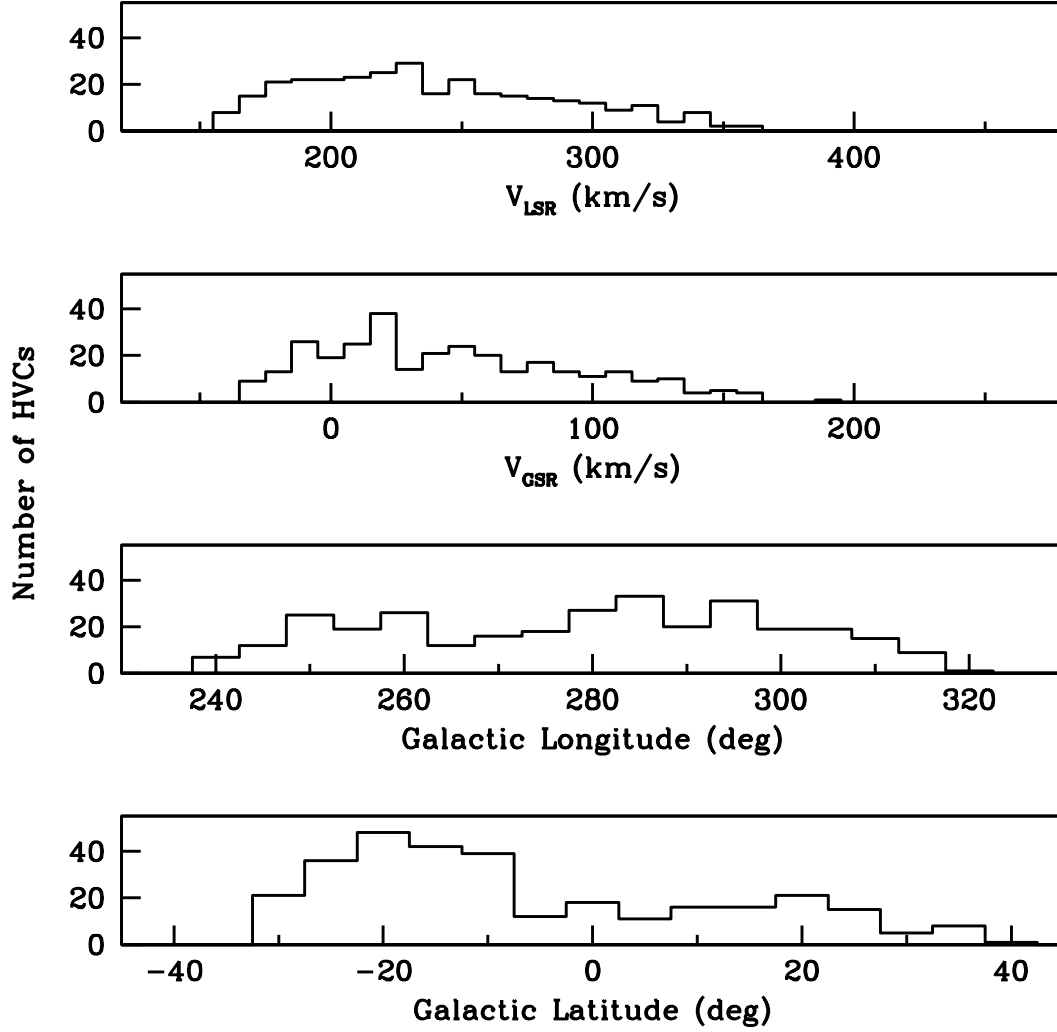


Fig. 11.— Histograms of  $V_{LSR}$ ,  $V_{GSR}$ , Galactic longitude and Galactic latitude of HVCs identified in the GASS data, from top to bottom, respectively. Excluded from the plot are: 30 clouds that extend below  $V_{LSR} = 150 \text{ km s}^{-1}$ ; 71 clouds that extend into the masked Milky Way emission boundary; 10 clouds that extend into the spatial edge of the image and galaxies.

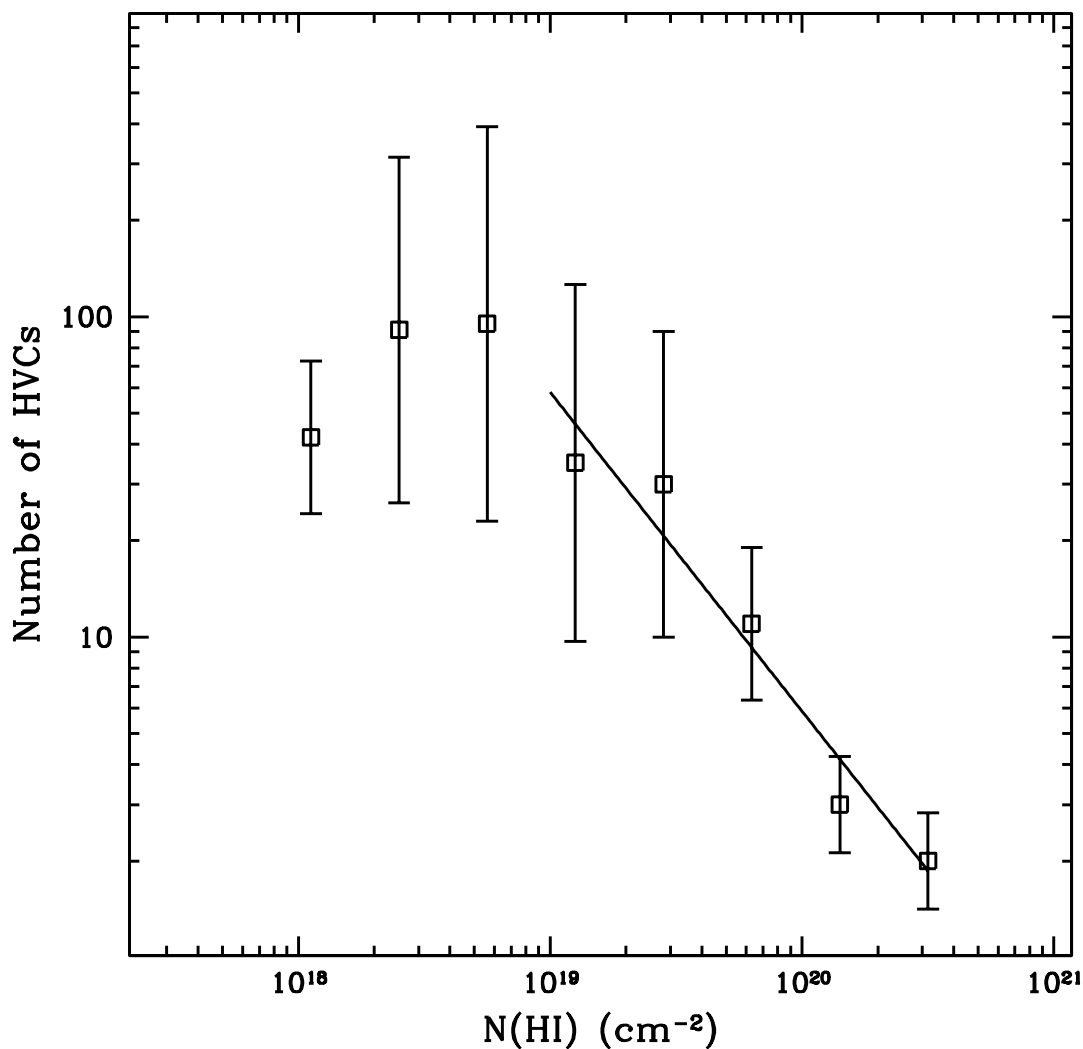


Fig. 12.— The peak HI column density distribution of HVCs in our catalog. A slope of  $-1.0$  is derived from least square fitting of the data points above  $10^{19} \text{ cm}^{-2}$  in the log-log plane, which corresponds to distribution function,  $f(N_{\text{HI}}) \propto N_{\text{HI}}^{-2.0}$ . Excluded from the plot are: 30 clouds that extend below  $V_{\text{LSR}} = 150 \text{ km s}^{-1}$ ; 71 clouds that extend into the masked Milky Way emission boundary; 10 clouds that extend into the spatial edge of the image and galaxies.

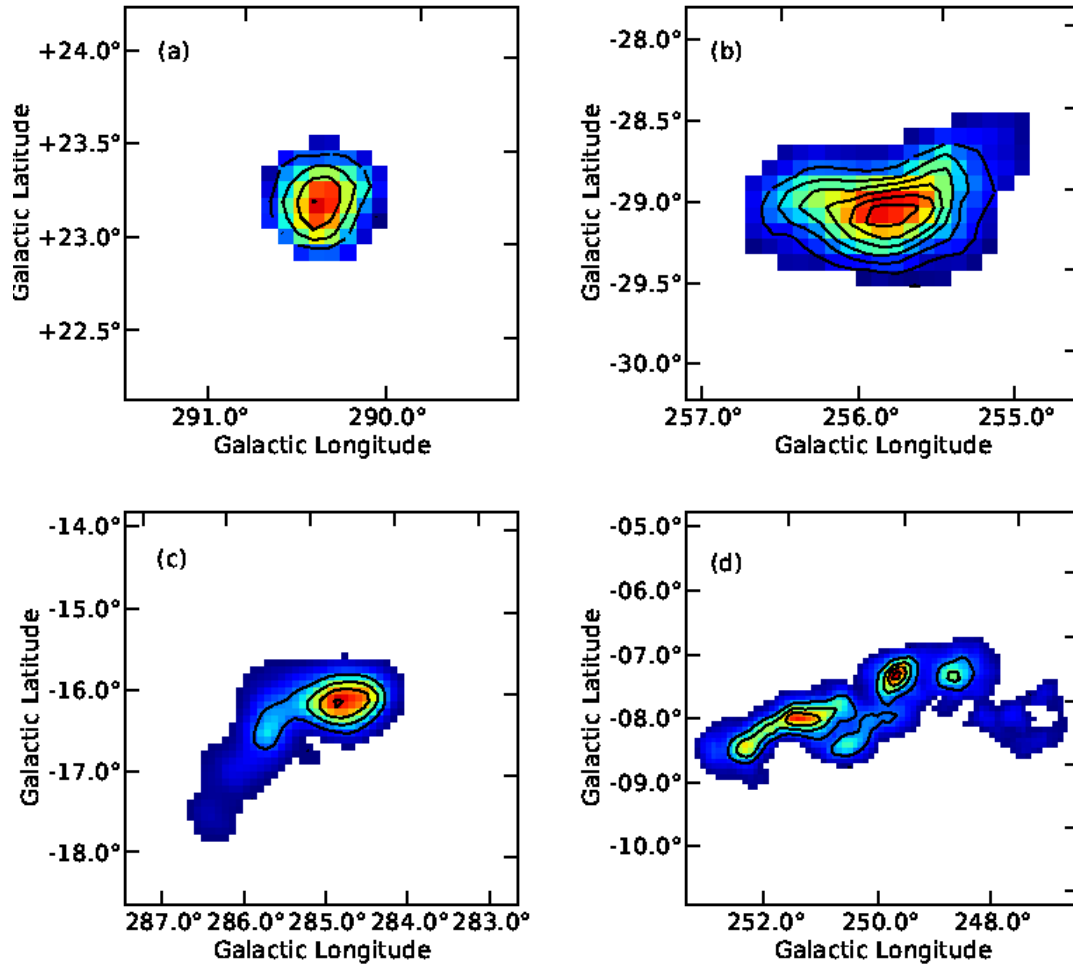


Fig. 13.— Examples of cloud morphological types: (a) symmetric cloud; (b) bow-shock shaped cloud; (c) head-tail cloud; (d) complex and irregular cloud.

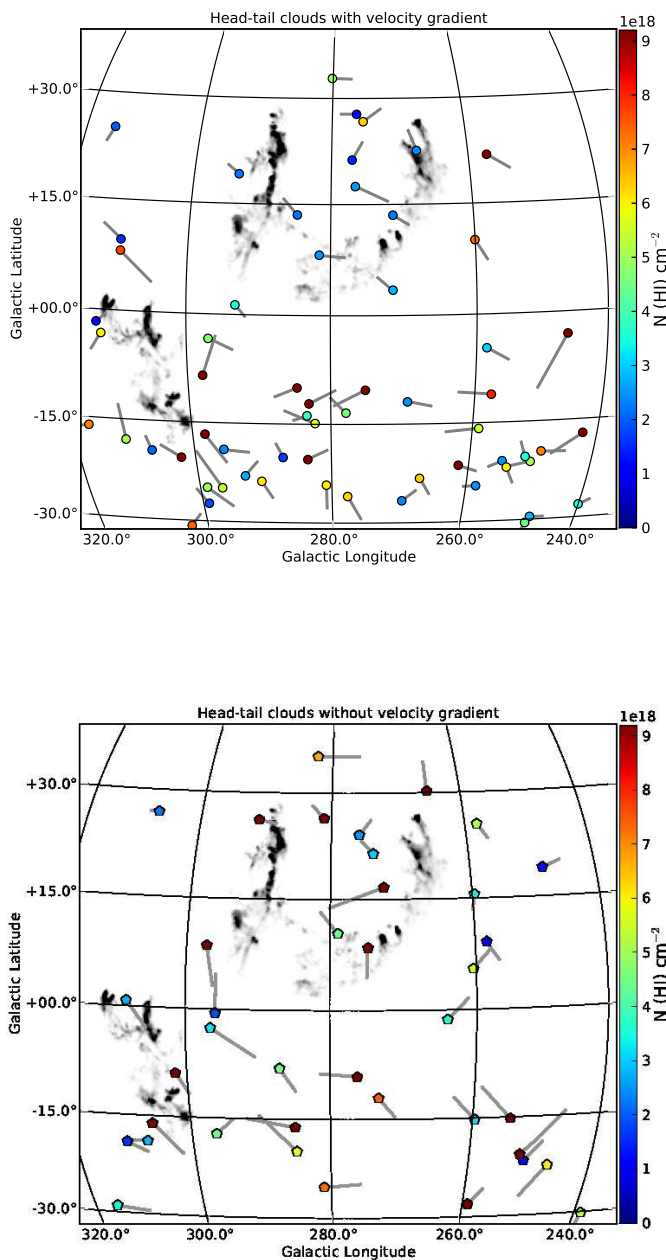


Fig. 14.— Sky distribution of identified head-tail clouds with velocity gradient (top panel) and without velocity gradient (bottom panel) in the region of the Leading Arm. The colors indicate the peak HI column density of each head-tail cloud according to the color bar scale on the right side. The head and tail have been enlarged from its original size in these plots. The derived position angle of head-tail clouds has been adjusted manually to represent the actual pointing direction whenever necessary (see §5.1).

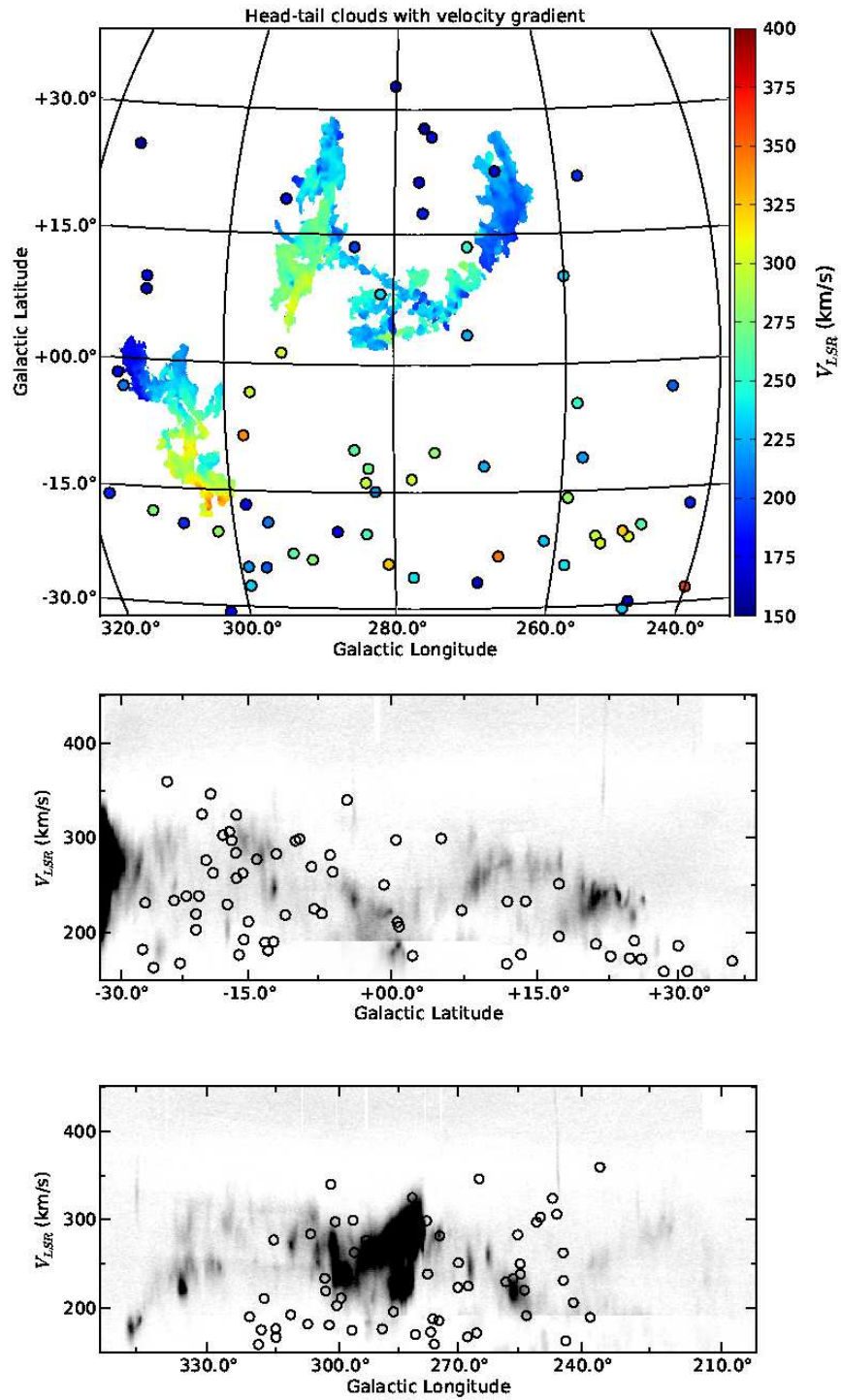


Fig. 15.— The top panel shows the sky distribution of identified head-tail clouds with velocity gradient (HT) in the region of the Leading Arm. The colors represent the  $V_{LSR}$  of each head-tail cloud according to the color bar scale on the right side. The bottom two panels show the HT clouds superimposed on position-velocity maps.

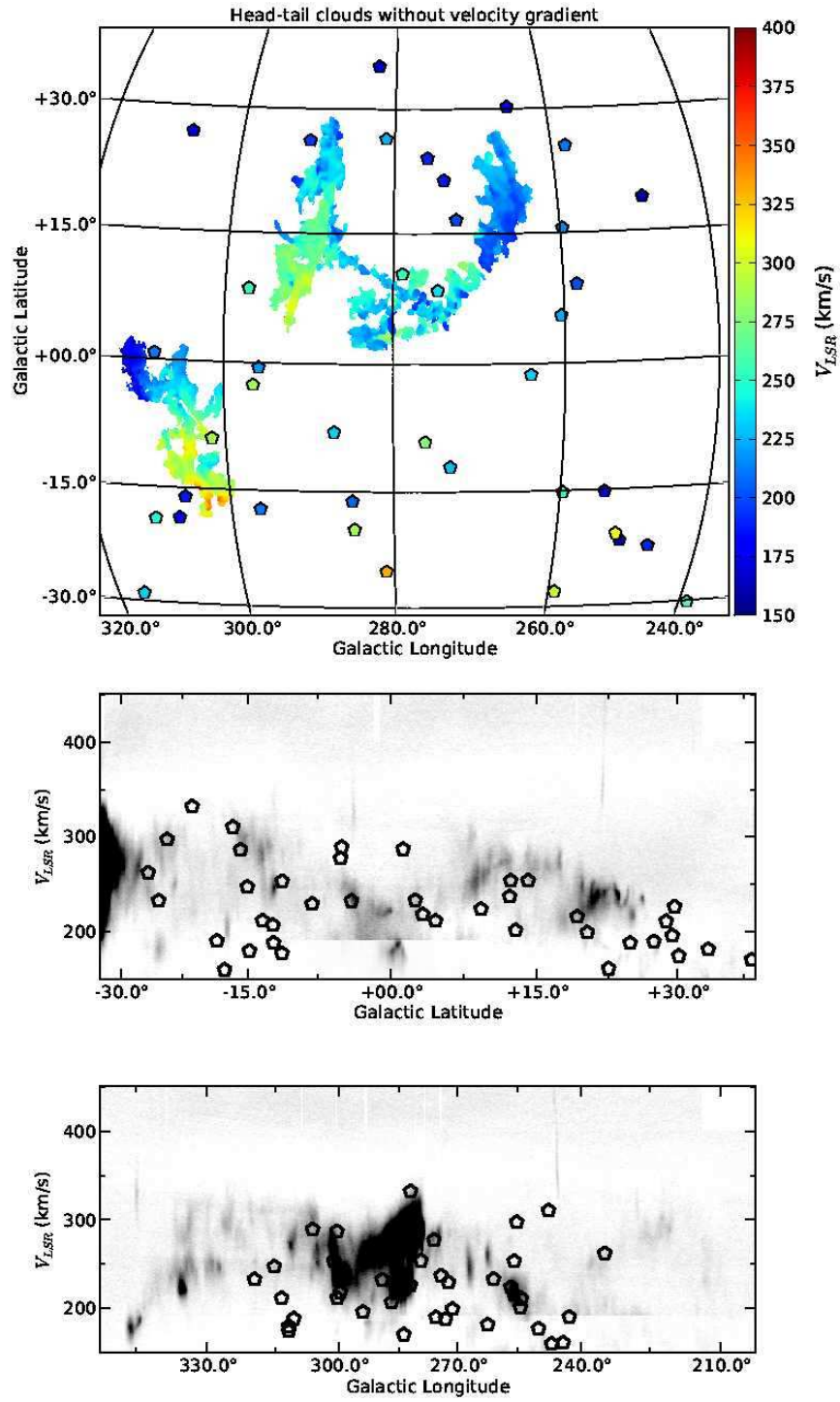


Fig. 16.— Same as Figure 15, except showing head-tail clouds without velocity gradients.



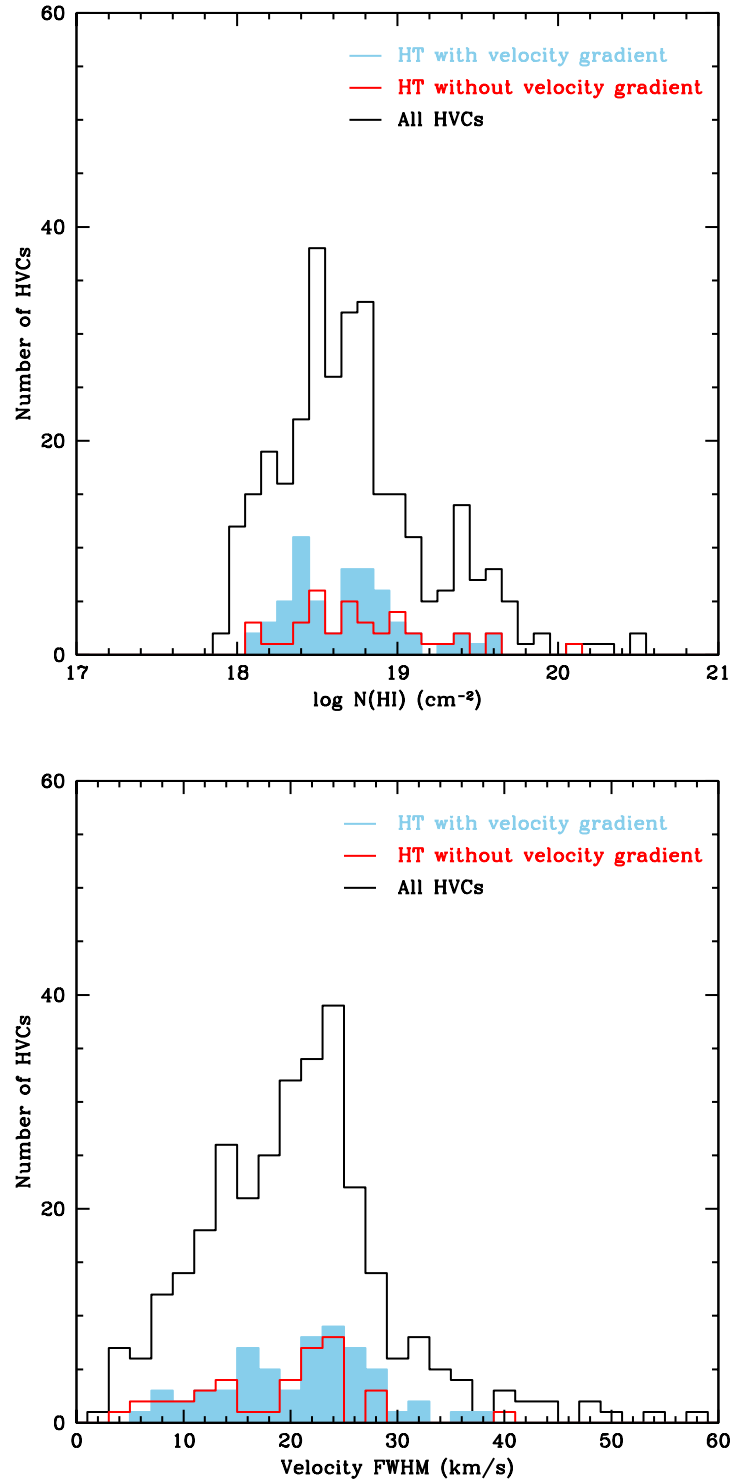


Fig. 17.— Histograms of peak HI column density (top panel) and velocity FWHM (bottom panel) of HVCs in this catalog. The black, blue and red represent all HVCs, head-tail clouds with velocity gradient and head-tail clouds without velocity gradient identified in GASS data, respectively. Only clouds with velocity FWHM less than  $60 \text{ km s}^{-1}$  are being plotted in the histogram.

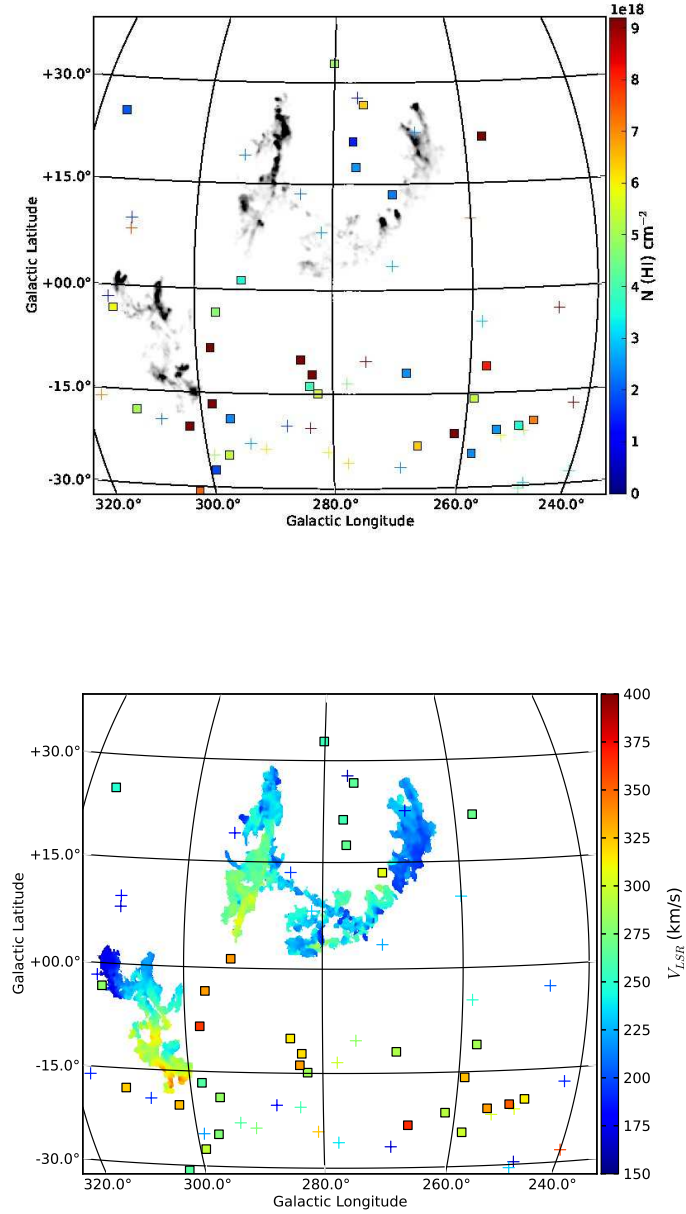


Fig. 18.— Sky distribution of head-tail clouds with positive velocity gradient (pHT; pluses) and with negative velocity gradient (nHT; squares). See definition in §5.1. The top and bottom panels show the distributions in peak HI column density and  $V_{LSR}$ , respectively. The colors indicate the values according to the color bar scale on the right side.

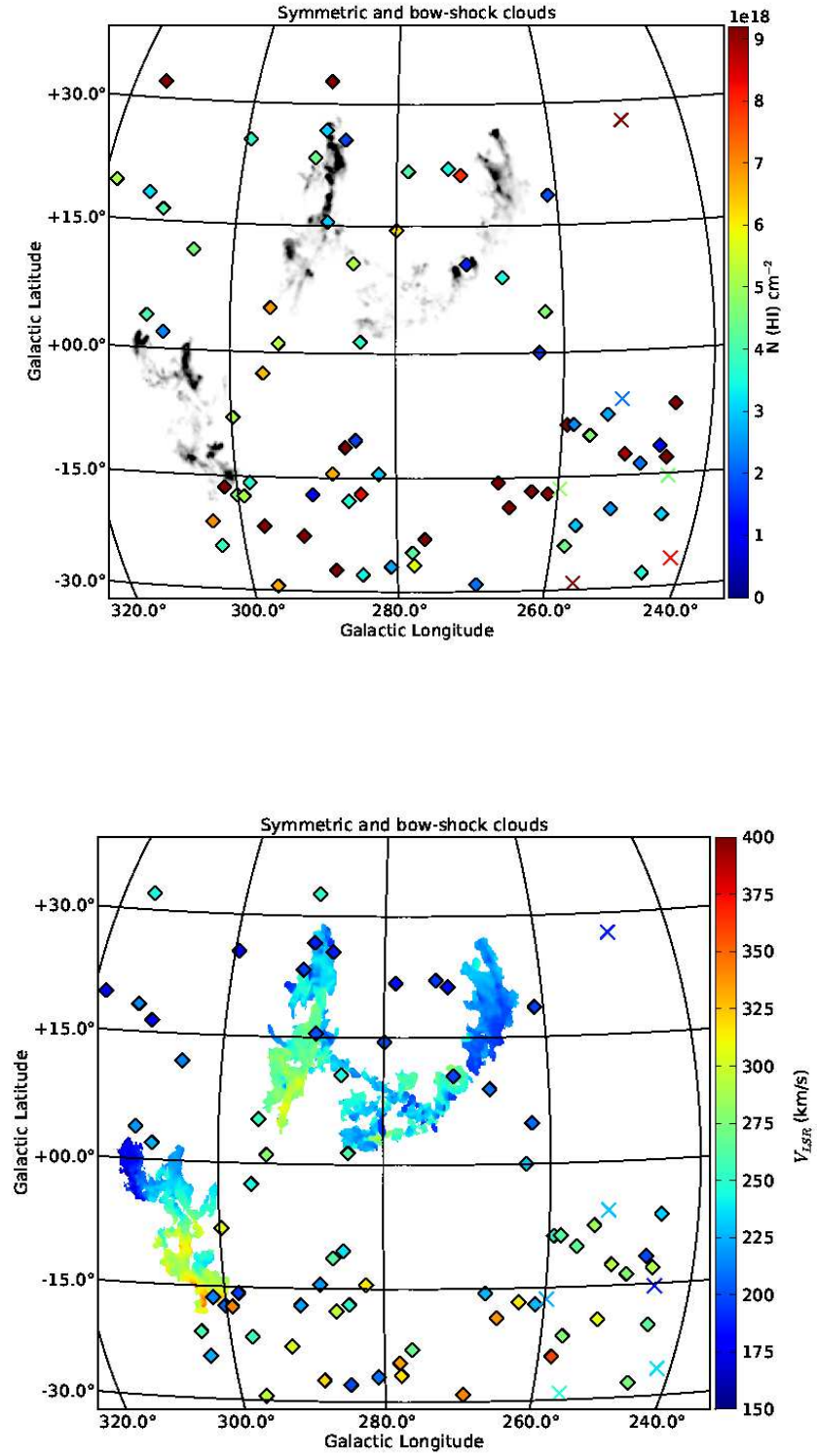


Fig. 19.— Same as Figure 18, except showing the sky distributions of symmetric (diamond) and bow-shock shaped clouds (crosses).

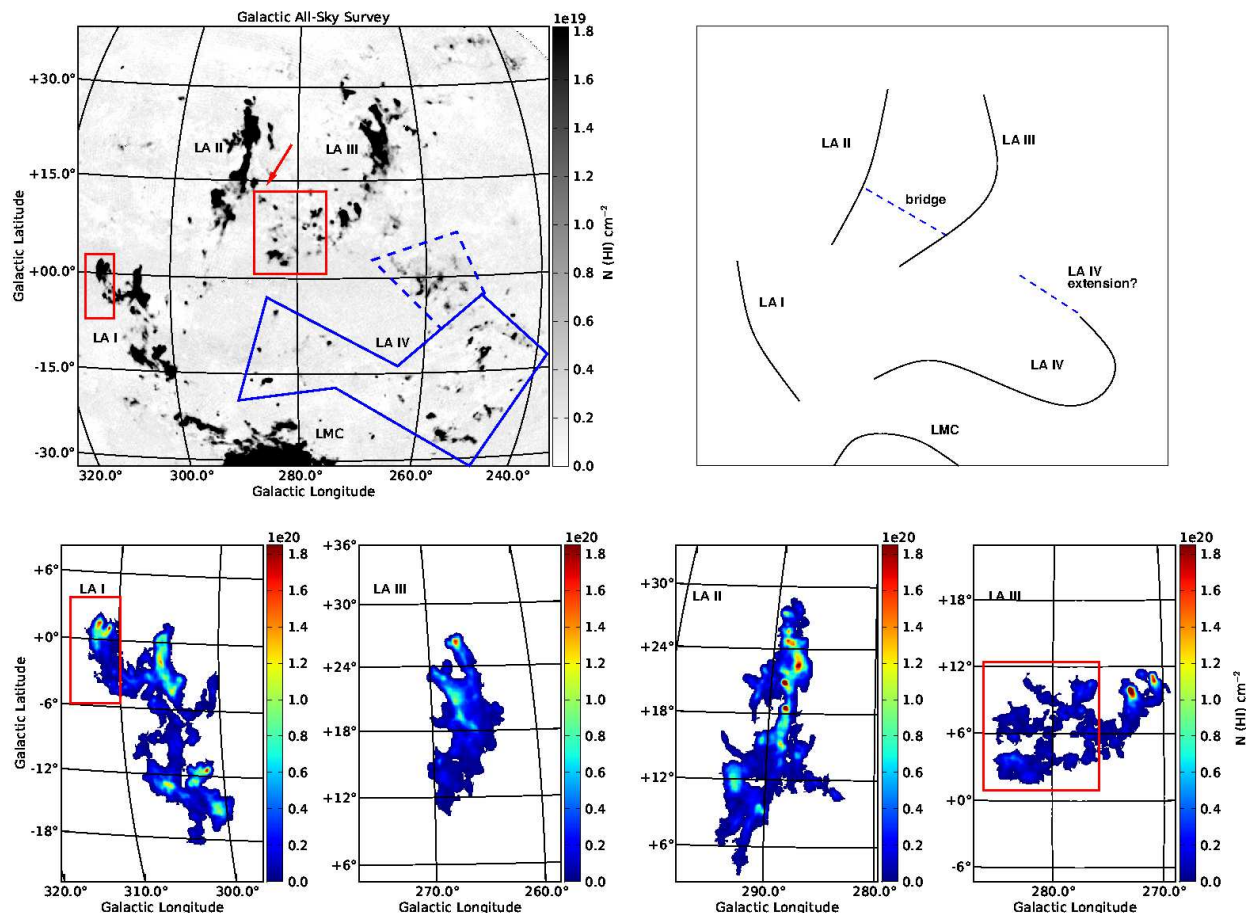


Fig. 20.— The top left figure shows the integrated HI column density map in the region of the Leading Arm. The red boxes highlight the extended features of LA complexes as seen in GASS. The arrow indicates the “bridge” structure connecting LA II and second cloud complex of LA III. The blue box shows the location of the new cloud population, namely LA IV. The blue dashed box marks the boundary of possible extended feature of the LA IV. The top right figure is a schematic diagram of the LA features and the LMC. The bottom subfigures show individual integrated HI column density maps of LA complexes as identified by *Duchamp*. The red boxes match the position as shown in the top figure.

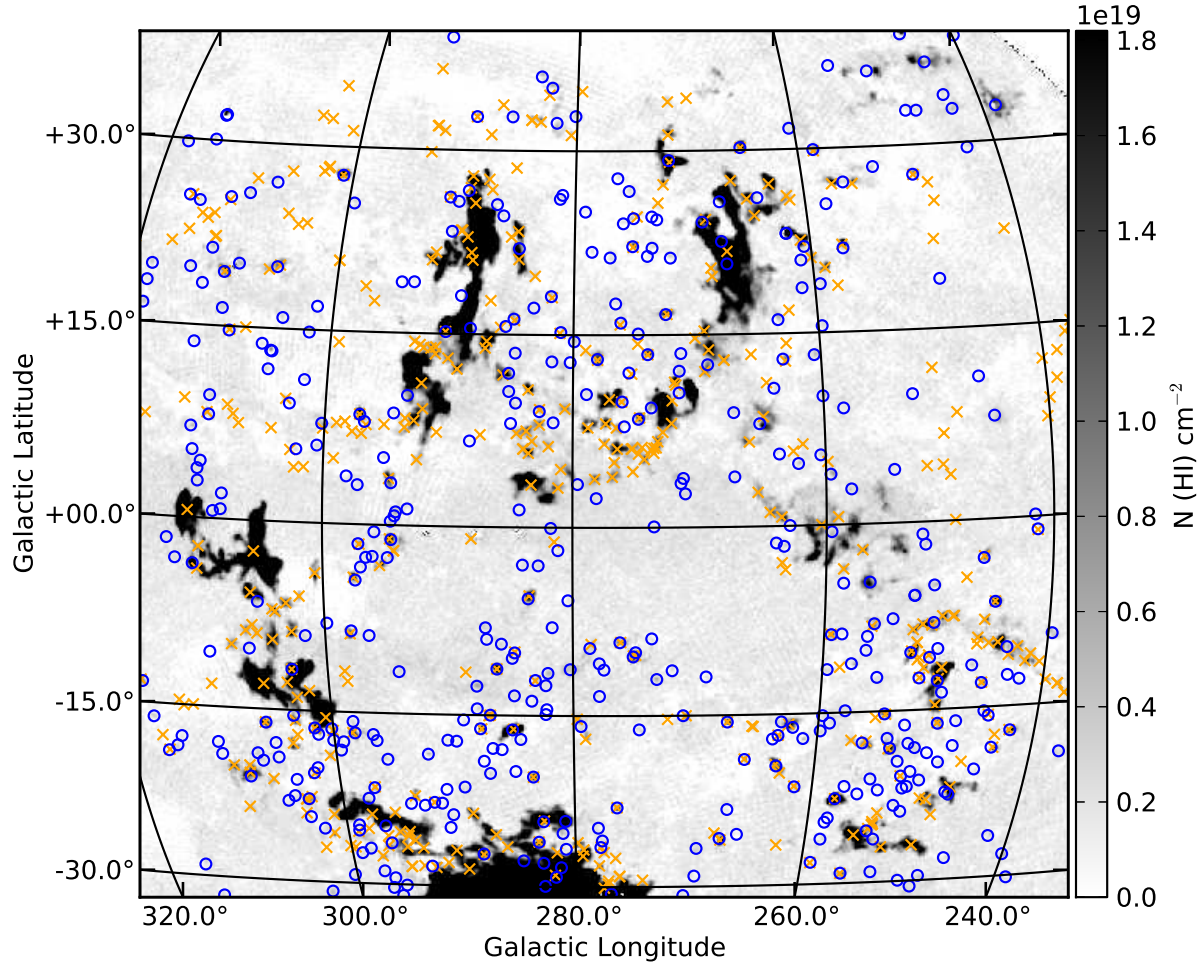


Fig. 21.— On-sky distribution of the 431 sources detected by *Duchamp* (blue circles) and the 433 sources detected by Venzmer et al. (2012) (orange crosses) in the same studied region of the Leading Arm. The integrated HI column density map of Figure 1 is shown. There is a slight difference in the studied velocity range of two catalogs.

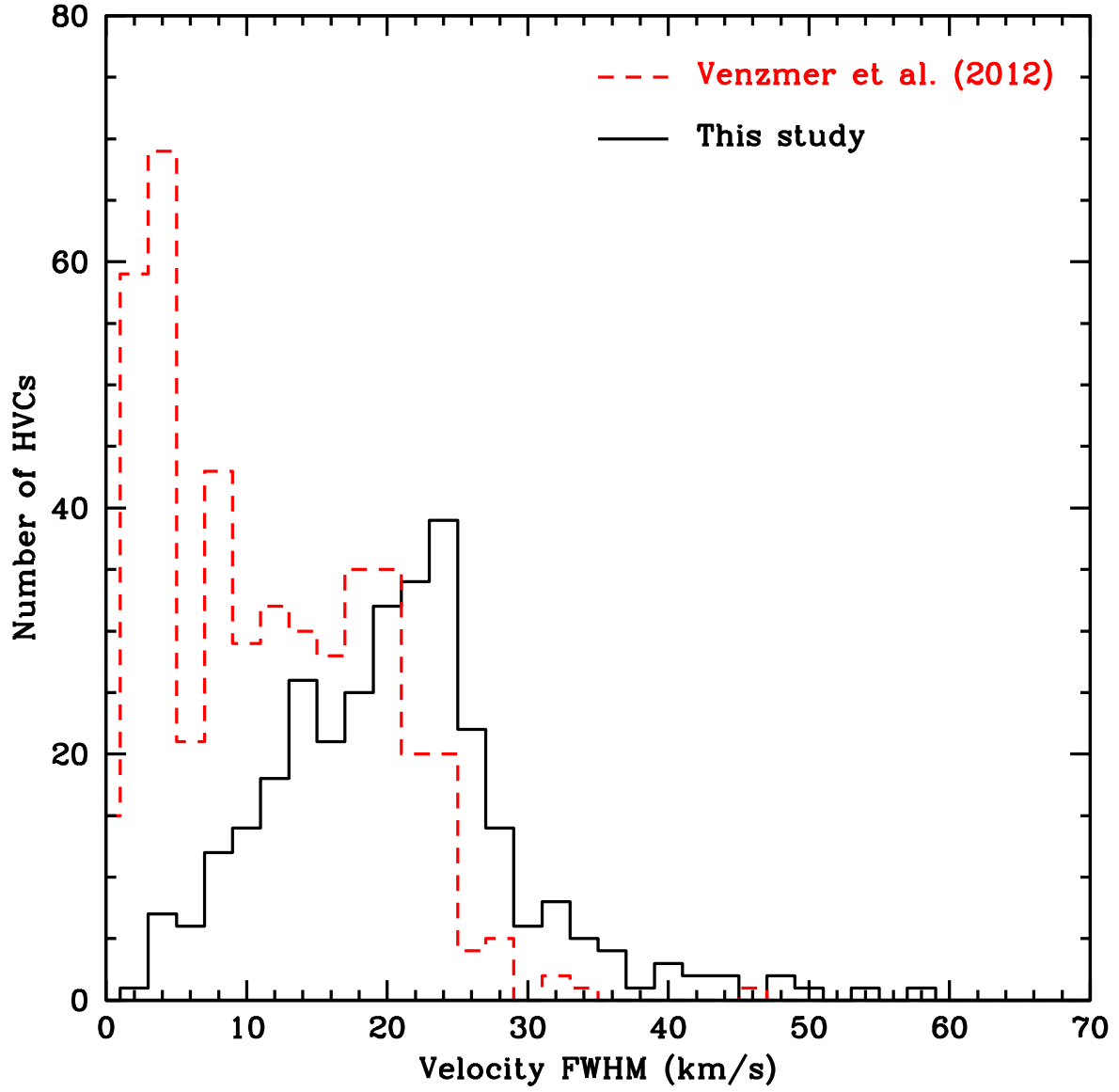


Fig. 22.— Similar to the bottom panel of Figure 17: histograms of velocity FWHM of HVCs in V12 (dashed line) and this study (solid line).

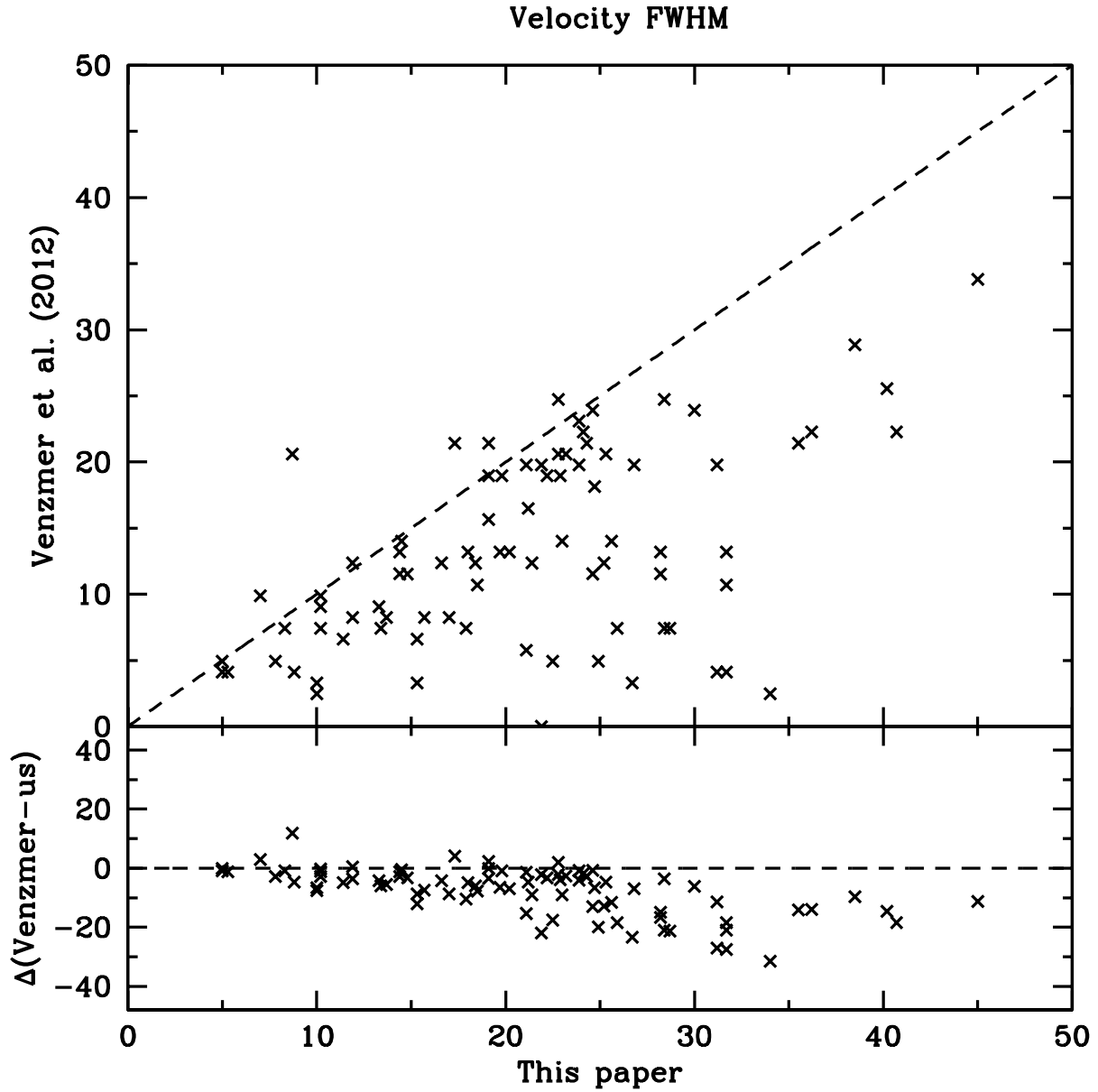


Fig. 23.— Comparison of our measured velocity FWHM with V12. The top panel shows 1:1 comparison of velocity FWHM measurements. The bottom panel shows the difference between our measurements and V12. One HVC with velocity FWHM larger than  $50 \text{ km s}^{-1}$  is not shown here.

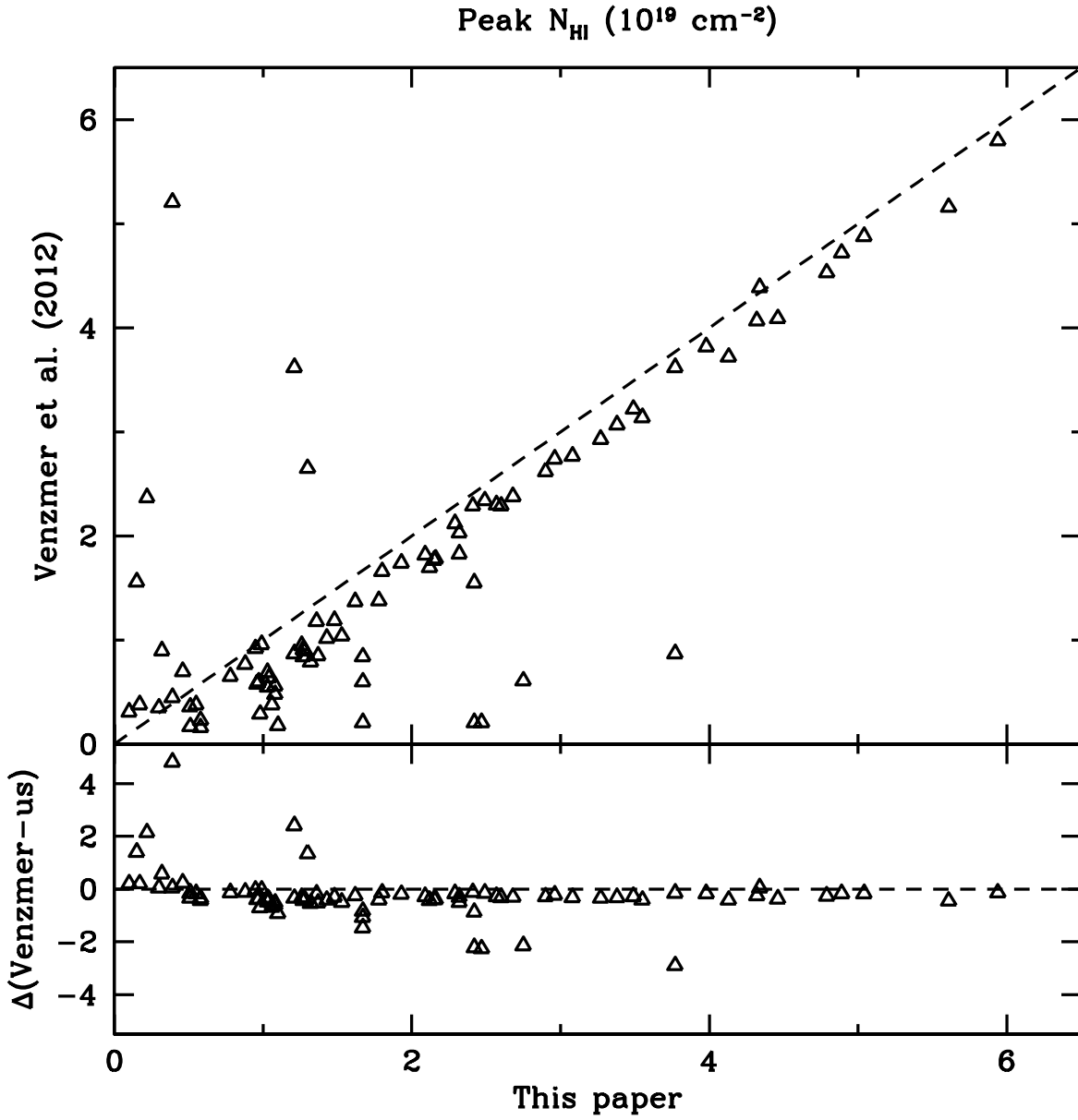


Fig. 24.— Same as Figure 23 except comparing peak  $N_{\text{HI}}$ . One HVC with peak  $N_{\text{HI}}$  larger than  $6 \times 10^{19} \text{ cm}^{-2}$  is not shown here.



Table 1. GASS catalog of detected sources in the region of the Magellanic Leading Arm.

ID	Designation	$V_{LSR}$	$V_{GSR}$	$V_{LGSR}$	FWHM	$F_{\text{int}}^{\text{a}}$	$T_{\text{B}}$	$N_{\text{HI}}$	Semi-major	Semi-minor	PA	Flag <sup>b</sup>	Classification <sup>c</sup>
(1)	( $gl \pm gb + V_{LSR}$ ) (2)	$\text{km s}^{-1}$ (3)	$\text{km s}^{-1}$ (4)	$\text{km s}^{-1}$ (5)	$\text{km s}^{-1}$ (6)	$\text{Jy km s}^{-1}$ (7)	K (8)	$10^{19} \text{ cm}^{-2}$ (9)	$^{\circ}$ (10)	$^{\circ}$ (11)	$^{\circ}$ (12)	(13)	(14)
63	HVC+236.9−19.1+174	...	...	...	...	...	...	...	...	...	...	M	IC
64	HVC+307.2+26.8+174	174.0	17.5	−60.2	12.4	2.1	0.20	0.23	0.2	0.2	−54	...	:HT
65	HVC+273.5+24.5+174	174.2	−25.6	−79.9	4.3	1.3	0.17	0.09	0.3	0.2	54	...	IC
66	HVC+251.3+36.6+175	174.5	7.3	−28.0	48.0	174.8	0.62	2.63	...	...	...	...	IC
67	HVC+293.3+19.1+175	174.8	−16.2	−85.5	11.5	3.1	0.20	0.22	0.3	0.2	35	...	HT
68	HVC+313.9−01.7+175	175.2	16.8	−54.0	8.7	1.5	0.21	0.12	0.3	0.2	−37	...	HT

Note. — Table 1 is published in its entirety in the electronic edition of the *Astrophysical Journal*. A portion is shown here for guidance regarding its form and content.

<sup>a</sup>Corrected  $F_{\text{int}}$ .

<sup>b</sup>SR: the detection lies at the edge of the spectral region; M: the detection extends over to the masked Milky Way emission region; E: the detection is next to the spatial edge of the image.

<sup>c</sup>HT: head-tail cloud with velocity gradient; :HT: head-tail cloud without velocity gradient; S: symmetric cloud; B: bow-shock cloud; IC: irregular/complex cloud.

